공학박사 학위논문

# Liquid Crystal-Based Tunable Diffraction Gratings and Polarization-Dependent Lens Arrays

## 액정 기반의 조정 가능한 회절격자 및 편광 의존 렌즈 어레이에 관한 연구

**2015 년 8 월**


서울대학교 대학원

공과대학 전기·컴퓨터공학부

김 지 윤

# Liquid Crystal-Based Tunable Diffraction Gratings and Polarization-Dependent Lens Arrays

지도교수 이 신 두

이 논문을 공학박사 학위논문으로 제출함

**2015 년 8 월**

서울대학교 대학원

공과대학 전기·컴퓨터공학부

김 지 윤

김지윤의 공학박사 학위논문을 인준함

**2015 년 6 월**

위 원 장 이 병 호 (인)

부위원장 이 신 두 (인)

위 원 박 남 규 (인)

위 원 유 창 재 (인)

위 원 최 윤 석 (인)

## Abstract

# Liquid Crystal-Based Tunable Diffraction Gratings and Polarization-Dependent Lens Arrays

Jiyoon Kim

Department of Electrical Engineering and Computer Science

The Graduate School

Seoul National University

In recent years, as the employment of optical systems such as display, communication, and data storage has expanded explosively, more sophisticated functions are required to these optical systems. Therefore, fundamental optical components playing significant role in the operation of these optical systems including diffraction gratings, lenses, beam splitters, prisms, and optical filters are widely studied in order to assign advanced and particular functions to optical devices. Among various fundamental optical components described above, the diffraction gratings and the lens arrays composed of regularly aligned lenses have been considered as key elements which are studied most widely due to their wide applications and relatively

simple operations and realizations. Since the tuning capability is essential for most recent optical systems, it is clearly required for the diffraction grating and the lens array to change the optical properties according to the external stimuli. For several decades, a number of types of tunable diffraction gratings and lens arrays have been suggested, and the optical properties of most of these devices were modulated by the applied electric voltage, the incident electromagnetic wave, or applied pressure. Especially, based on the large electro-optic modulation of liquid crystals (LCs) resulting from the high optical anisotropy and the electrically or optically tuning capability, a variety of tunable diffraction gratings and lens arrays using LC have been suggested. However, LC diffraction gratings suffer from the very limited diffraction pattern due to the difficulty in achieving unconstrained alignment, or the slow and small change in the diffraction characteristics when optically controlled. Furthermore, the applications of LC lens arrays are also limited owing to the sensitivity of LC alignment on the geometrically uneven substrate or the restricted focusing effect compared to other types of lens.

This thesis primarily aims to demonstrate new types of LC diffraction gratings and LC lens arrays. It consists of three major categories, first one and the second one of which concern the electrically tunable LC grating, and the optically tunable ferroelectric LC (FLC) grating. The last one concerns the electrically tunable LC square lens array and the LC lenticular lens array.

Firstly, a fully continuous LC grating device with the alternating semi-circular alignment which exhibits the switching effect between the diffraction orders independent of the thickness of the LC cell is demonstrated. The

continuous phase modulation in the LC grating with the rotational symmetry was achieved on a micro-imprinted surface where the semi-circular alignment of the LC was spontaneously produced. This LC grating device in the hybrid geometry exhibited the perfect continuity of the phase retardation and the switchable diffraction as a function of an applied voltage. It was also found that the symmetry of the input polarization direction with respect to the grating patterns results in the interchange between two symmetric grating configurations.

Secondly, an all-optically switchable FLC grating constructed in an alternating binary configuration with different optical properties from domain to domain is demonstrated. A dye-doped FLC is uniformly aligned in one type of domains whereas it is infiltrated into the photo-polymerized networks of reactive mesogens in the other. Compared to conventional nematic LC cases, this FLC-based grating allows more efficient all-optical modulation and faster diffraction switching in subsecond since the optical response associated with the dye molecules in the layered state is less hindered than in the orientationally ordered state.

Finally, an LC-based square lens array with two focusing modes according to the polarization state of the input light is demonstrated. The homogeneously aligned LC layer is placed on an array of static square lenses fabricated using a photo-curable polymer whose refractive index is matched with the refractive index of the LC. For the input beam polarized parallel to the easy axis of the LC, the focal length is varied with the applied voltage. For the perpendicularly polarized input beam, the focal length is independent of

the applied voltage and remains constant. An LC-based lenticular lens array, having a polarization-dependent focusing effect, fabricated through a simple imprinting process is also demonstrated. The input polarization-dependence of our LC lenticular lens array arises mainly from the index matching scheme between the polymer lenticular lens and the LC on it.

In conclusion, throughout this thesis, new types of LC diffraction gratings including electrically tunable LC grating having continuous alignment geometry and optically switchable FLC binary grating with superb switching capability are demonstrated. Moreover, electrically tunable LC square lens array and LC lenticular lens array with perfect polarization-dependence are also described. These advanced fundamental optical devices will be useful for devising a variety of sophisticated optical systems.

**Keywords: Diffraction grating, Lens array, Nematic liquid crystal, Dye-doped ferroelectric liquid crystal, Reactive mesogen, Imprinting**

**Student Number: 2009-20783**

# Contents

# List of Figures

# Chapter 1. Introduction

## 1.1. Diffraction Gratings and Lens Arrays

In recent days, a number of optical systems such as optical signal processing, optofluidic systems, optical sensing, and displays require more sophisticated and elaborate functions. These systems consist of diverse fundamental optical components playing critical roles including optical gratings, lens, prisms, beam splitters, optical filters, and so on. Therefore, for realizing more advanced optical systems, optical components with particular characteristics have been studied widely. Among various fundamental optical components described above, the optical grating and the lens arrays having a lot of lenses aligned regularly are considered as key components due to their wide applications and relatively simple realizing and fabrication. In this chapter, the basic information and researches about the optical gratings and lens arrays are introduced briefly.

Optical diffraction grating is an optical component with a periodic structure playing a role of splitting and diffracting incident beam into multiple beams in different directions. The direction and the intensity of diffracted beam can be determined freely by the structure of the grating element according to their purpose of use. Due to this capability of selecting the direction and intensity of beam, the optical grating components were commonly used in monochromators and spectrometers at first. However, as

various types of optical systems are developed explosively, the applications of the gratings expanded to optical data storage, optical communication, and display systems.

Optical gratings can be divided into transimissive and reflective types. The schematic diagrams of transmissive type and reflective type gratings are shown in Fig. 1.1. As shown in this figure, the diffracted beams of the transmissive type are separated from the transmitted beam through the grating element (0th order), whereas the diffracted beams of the reflective type are separated from the reflected beam from the grating element (0th order). The angle between *m*th order and 0th order of diffracted beam $\theta_m$ determines the propagating direction of diffracted beams and this value can be calculated by the grating equation. The grating equation can be expressed as [1]

$$\Lambda \sin \theta_m = m\lambda \,. \tag{1.1}$$

Here, $\Lambda$ and $\lambda$ denote the period of grating element and the wavelength of incident beam, respectively. Based on this equation, if the beam incident at angle of $\theta_i$ with respect to the grating element, the direction of *m*th order of diffracted beam can be calculated as

$$\theta_m = \arcsin(m\lambda / \Lambda - \sin \theta_i) \,. \tag{1.2}$$

These equations mean that the direction of diffracted lights can be adjusted freely by modulating $\lambda$ and $\Lambda$.

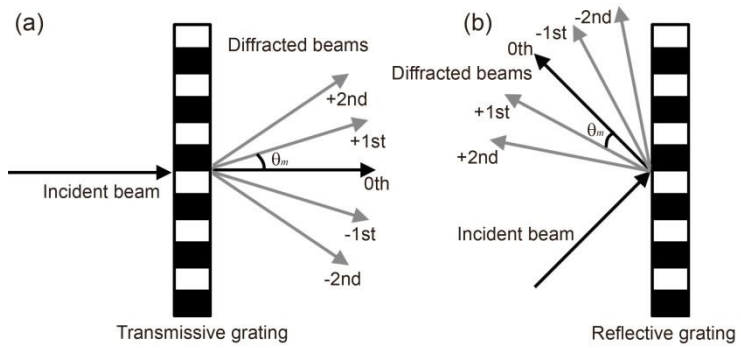


**Figure 1.1.** Schematic illustration of (a) transmissive diffraction grating and (b) reflective diffraction grating.

The intensity of diffracted beam can be also changed by modulating grating structure. By Fraunhofer diffraction approximation, the diffraction pattern $I(x,y)$ of the light $I_i$ passing though light aperture having aperture function of $p(\xi,\eta)$ can be calculated as [1,2]

$$I(x,y)=\frac{I_i}{(\lambda d)^2}\left|\int\int_{-\infty}^{\infty} p(\xi,\eta)\exp[j2\pi(\frac{x}{\lambda d}\xi+\frac{y}{\lambda d}\eta)]d\xi d\eta\right|^2 . \qquad (1.3)$$

In this equation, $d$ means the distance of observation from the aperture. Note that the light intensity of diffraction patterns is proportional to Fourier transform of the aperture function as shown in Eq. (1.3). Therefore, if the light aperture is an optical grating having periodic structure in nearly infinite domain, the diffraction pattern will have discrete function. A Fourier transform of periodic function with infinite domain of definition can be expressed as series of Dirac delta functions with amplitude of Fourier coefficients. Thus, the intensity of $m$th order of diffracted light of the 1-

dmenstional optical grating $D_m$ with the aperture function of $T(x)$ with period of $\Lambda$ can be expressed as [1,2]

$$D_m = \frac{I_i}{\Lambda^2}\left|\int_{-\infty}^{\infty} T(x)\exp(-2im\pi/\Lambda)dx\right|^2. \tag{1.4}$$

By constructing various optical grating with different aperture functions, numerous diffraction patterns with different efficiencies are obtainable.

A lens is a transmissive optical element which affects the focusing of a light beam through refraction. A simple lens usually fabricated by curved form of optically transparent materials. Rays are refracted by different direction according to the angle between a ray and the surface of a lens where the ray passes through, and this makes a focusing effect. Since the focusing of light is very important and fundamental function in almost every optical device, the application of the lens is very broad compared to other basic components. Furthermore, if a lot of lenses are aligned regularly, their use can be expanded to three-dimensional (3D) displays, optical communication systems, and optical tweezers.

A schematic structure of a simple lens is shown is Fig. 1.2. In this figure, $R_1$ and $R_2$ mean radius of curvature of the lens surface closest to the light source and farthest form the light source, respectively. The focal length $f$ of this lens is approximated as [2]

$$f = (n-1)\left(\frac{1}{R_1} - \frac{1}{R_2}\right). \tag{1.5}$$

In this equation, $n$ denotes the refractive index of material composing the lens. Since the focal length is the most critical factor in designing lens structure,

there have been many researches on diverse lens structure for realizing varied focusing effects with sufficient focusing efficiency.

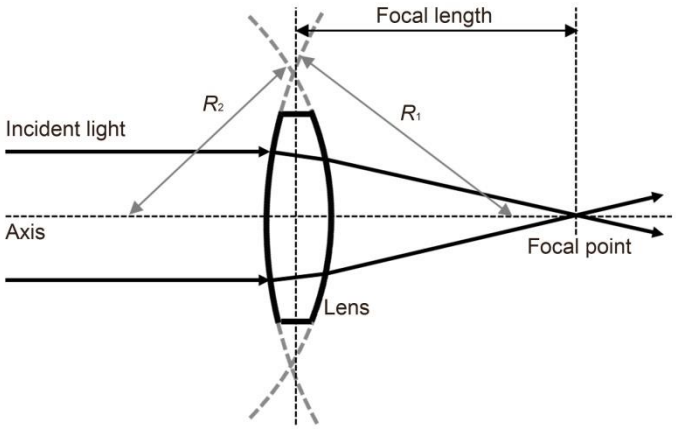


**Figure 1.2.** Schematic illustration of typical convex lens.

Lenses can be divided into spherical type, and cylindrical type and so on according to their shape. Since the spherical type is the most widely used structure which having circular lens aperture, its application is very broad in optical systems. The cylindrical type has a square-shaped aperture and its applications are easily found in 3D displays such as lenticular lens arrays and integral imaging systems. Lenses can be also divided into conventional type, Fresnel type, gradient refractive index (GRIN) type, and so on as shown in Fig. 1.3 according to their focusing principles. Unlike conventional lenses in Fig. 1.3(a), Fresnel lenses have their optical surface broken up into very narrow slices, allowing lenses to be much thinner and lighter, and GRIN

lenses have flat optical surfaces, but have a radial or axial variation of refractive index that causes light passing though the lenses to be focused.

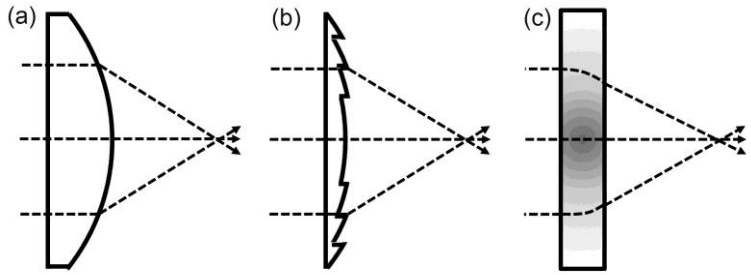


**Figure 1.3.** Schematic diagrams of (a) conventional lens, (b) Fresnel lens, and (c) GRIN lens.

## 1.2. Tunable Optical Devices

### 1.2.1. Tunable Diffraction Gratings

For the realization of advanced optical devices based on grating elements, the tunable grating which changes its diffraction property according to the external stimulus is very essential. Various kinds of stimuli such as electrical voltage, electromagnetic wave, or physical pressure can be used as the stimuli for the tunable optical gratings. Among grating devices based on these stimuli, the electrically tunable optical grating is the most widely studied and suggested tunable gratings due to their compactness and the advantages in direct applications for electro-optical devices. These gratings change the

period or geometry according to the applied voltage. Therefore, the electrically responsive materials are essential in fabricating these types of gratings. Especially, liquid crystals (LCs) are widely used for optical devices due to the large electro-optic modulation resulting from the high optical anisotropy, the electrically tuning capability at low voltages, and the design flexibility. The response of electrically tunable LC grating is discussed in **Chapter 3** in detail. The optically tunable optical gratings are also widely studied recently. These gratings usually respond to the electromagnetic wave whose wavelength λ is in the range of 200 ~ 700 nm, and are usually fabricated by the photoresponsive materials. For example, dye-doped monomers or polymers are very promising candidate for the optically tunable gratings due to the dynamic and fast response and the potential for simple applications. Moreover, these gratings have capacity for wavelength selection meaning that they response differently under the irradiation of light with different wavelength. The response of optically tunable LC grating is discussed in **Chapter 4** in detail. Finally, physically tunable gratings are fabricated by flexible materials which are deformed by the pressure or materials which change their electro-optical properties according to the external pressure. These gratings are usually applied to waveguides or optofluidic devices.

### 1.2.2. Tunable Lens Arrays

Since the lens is the very fundamental optical component which focuses the light beam, tunability in focal length or switchability of focusing effect are very important factors to expand the application of lenses. Being similar to the grating elements described above, the tunability can be realized by the physical deformation of lens surface, or the electrically or optically responsive change of optical properties of materials composing lenses. Physically tunable lenses are usually fabricated by the flexible and transparent materials, and the radius of curvature is adjusted by modulating the external or internal pressure. In other words, the focal length is changed by the physical deformation of lens surface. Electrically tunable lens are composed of electrically responsive material which change their optical properties according to the applied voltage. For example, LC-based lenses are widely studied due to their compactness, easy fabrication, and high optical anisotropy. Especially, compared to other types of lens, electrically tunable lens has overwhelming advantages in fabricating micro-lens arrays which can be applied to 3D displays, optical data storages, optical communications, and optical tweezers. The structures and operation of electrically tunable LC lens is discussed in **Chapter 5** in detail. The optically tunable or switchable lenses which are fabricated with photoresponsive materials are also demonstrated.

## 1.3. Outline of Thesis

This thesis contains six chapters including this **Introduction** and **Concluding Remarks**. In **Chapter 1**, fundamental optical components, especially optical gratings and lenses are introduced briefly, and simple equations related to the diffraction direction and the diffraction efficiency of the diffraction grating, and the focal length of the lens are also introduced. Additionally, several types of operation principles of tunable optical gratings and tunable lenses including the applied electric voltage, the incident electromagnetic wave, and the applied pressure are described. **Chapter 2** explains the theoretical background with regard to the LCs. At first, the basic optical properties of LC are introduced. The basic structure and optical and physical properties of the phases of the thermotropic LCs including nematic, smectic A (SmA), smectic C (SmC), and chiral smectic C (SmC*) phases are also discussed. In order to assist the understanding of LC-based devices demonstrated in this thesis, the basic alignment processes which determine the direction of LC molecules and some basic LC cell geometries induced by different alignments of LC are introduced briefly. After that, the electric field-induced and the light-induced reorientation of LC molecules which have very close relation with the principle of the LC-based optical devices demonstrated in this thesis are discussed. In **Chapter 3**, an electrically switchable fully continuous LC diffraction grating device based on the semi-circular LC alignment is demonstrated [3]. This grating device has periodic LC domain aligned on the periodic microgroove structure, and the microgrooves were constructed using a simple imprinting technique. The LC molecules were aligned stably along the microgroove, and the diffraction properties were tuned by the applied

electric voltage. The measured diffraction efficiencies were found to agree well with the theoretical predictions made in the transfer matrix formalism. In **Chapter 4**, an optically switchable ferroelectric LC (FLC) binary grating is demonstrated [4]. This FLC grating consists of the optically isotropic stable region and the optically anisotropic tunable region. In order to construct the polymer structure composing stable region, a reactive mesogen (RM) was used, and a dye-doped FLC was used as the photoresponsive material composing tunable region. Compared to the dye-doped nematic LC (NLC), the dye-doped FLC showed the larger and faster change in optical properties. Based on this characteristic of the dye-doped FLC, an optically tunable diffraction grating with superb switching capability was fabricated stably. **Chapter 5** consists of two parts demonstrating polarization-dependent LC lens arrays. One part is about the square LC lens with fully activated area [5]. This lens array consists of polymer convex lens array and the injected LC layer. By matching the refractive index of polymer and the refractive index of the extraordinary axis of LC, this lens array was able to show the superb polarization-dependence and the focusing effect. A simple experiment showing the image selection according to the polarization state is also included. The other part is about the polarization-dependent LC-based lenticular lens array [6]. Similarly to the LC square lens array described briefly above, the lenticular lens showed excellent polarization-dependence through the index-matching between the long axis of the LC and the polymer. The application to the two-dimensional (2D)/3D switchable display was also suggested briefly. Especially, in these two lens arrays, the LC molecules were

aligned unidirectionally without any additional alignment layer. Finally, **Chapter 6** provides the summary and the concluding remarks.

# Chapter 2. Theoretical Background

## 2.1. Basic Properties of Liquid Crystals

### 2.1.1. Liquid Crystals

LC is a matter in state that has properties between those of conventional liquid and those of solid crystal. Basically, molecules in liquid phase are randomly distributed in space without any positional and directional order, whereas molecules in solid crystal are fixed in certain place with both positional and directional order. Since LC is intermediate state between these two states, it has fluidity of liquid state as well as directional order of molecules of solid state. The basic difference among states of matter is that the constituent molecules are arranged in different geometrical configurations under different thermodynamic conditions. In general, external conditions such as temperature, specific molecular interactions determine the possible configurations of the given systems.

Basically, LCs are anisotropic fluid. They combine fluidity generally observed in liquids and anisotropic physical properties as observed in crystalline state. They represent thermodynamically stable phases situated between isotropic liquids and the crystalline solids. In general, LCs are divided into thermotropic, lyotropic, and metallotropic types. Thermotropic and lyotropic LCs consist of organic molecules. Thermotropic LCs exhibit a

phase transition as temperature is changed. Lyotropic LCs exhibit phase transitions as a function of both temperature and concentration of the LC molecules in a solvent. Metallotropic LCs are composed of both organic and inorganic molecules, and their phase transition depends not only on the temperature and the concentration, but also on the inorganic-organic composition ratio.

Among various particular properties which LCs have, the anisotropy is the most important property for their applications. The anisotropy in dielectric constant makes LC change their alignment direction according to the applied electric field or the incident electromagnetic waves and the anisotropy in refractive index makes LC respond differently according to the polarization state of the incident light or affect the polarization state of the incident light. Due to the unique and intriguing properties, LCs have been used and studied widely in numerous fields of science such as optics, electronic engineering, fluidic dynamics, and so on.

### 2.1.2. Phases of Liquid Crystals

Before introducing phases of thermotropic LCs, note that even though the shapes of LC molecules are complicated, they are referred to as rod-like shape as shown in Fig. 2.1. The electrical and optical anisotropy described above comes mainly from this uniaxially anisotropic rod-like shape of LCs. Therefore, the long axis of LC is called extraordinary axis, and the short axes are called ordinary axes. In general, LC molecules tend to align parallel to

each other on the average leading to a preferred direction in space. There exist LCs which doesn't have rod-like shape, of course, but they are not of interest in this thesis.

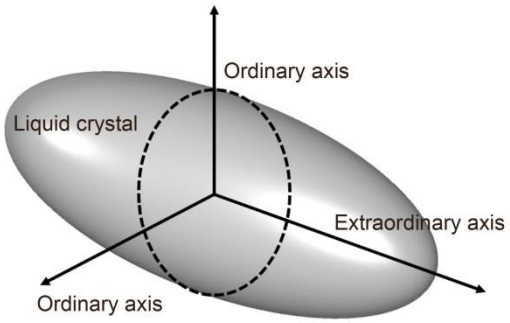


**Figure 2.1.** Schematic illustration of LC molecule and optical axes.

Thermotropic LCs can be divided into some phases according to their directional or positional alignment order. Four typical phases of LCs are shown in Fig. 2.2. In the nematic phase, the extraordinary axes of LC molecules are aligned, on average, parallel to a particular direction which can be indicated by a global unit vector **n** called director. In principle, the direction of the **n** vector is arbitrary in space and represents the direction of the optic axis of the system. The nematic phase possesses an orientational order, but no positional order in a long range. Only the long axis of the molecules is more or less oriented, but there is a random distribution between the heads and the tails of the molecules. The nematic phase is therefore optically uniaxial. The measure of the degree of order in nematic phase is given by the order parameter *S* [7,8]

$$S = \frac{3}{2}\cos^2 \omega - \frac{1}{2} \tag{2.1}$$

where ω is the deviation angle of individual molecules from the director. For example, in case of isotropic liquid, the value of *S* is 0, and in case of perfect orientational order such as solid, *S* is 1. Normally, LC has value of *S* between 0.5 and 0.7, and this value decreases as the temperature increases.

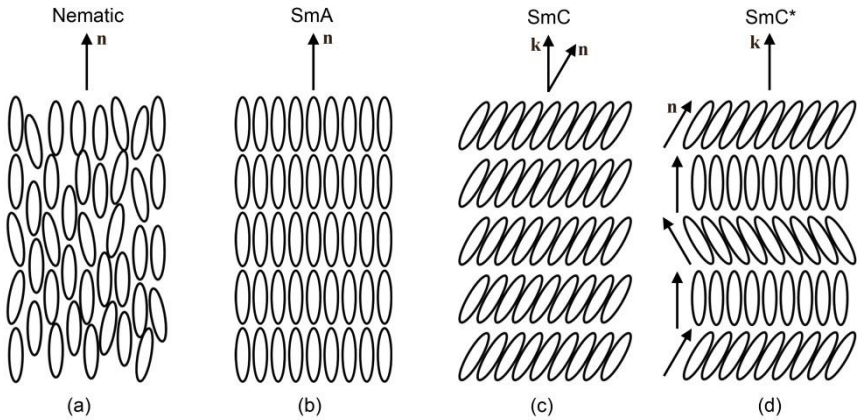


**Figure 2.2.** Schematic illustration of (a) nematic, (b) SmA, (c) SmC, and (d) SmC* phase of thermotropic LC.

On lowering the temperature of a nematic phase, additional features of order may appear, like positional order of the molecules' center of mass. This leads to the layered structure such as SmA, SmC, and chiral SmC* phases, which are regarded as two dimensional liquids. In the SmA phase, molecules are oriented more or less parallel to each other and their position is ordered in layers, in which the layer spacing is approximately equal to the length of the molecules as shown in Fig. 2.2(b). It means that there exists a degree of

positional order, determined by the formation of so-called smectic layer. The director in the SmA phase is normal to the smectic layers and determines the optic axis. Although the layers are not strictly defined in reality, a plot of the density of centers of mass $\rho_s$ versus distance along the axis parallel to the director usually follows a sinusoidal variation as

$$\rho_s(x) = \rho_0\left(1 + \psi \sin\left(\frac{2\pi z}{d_0}\right)\right). \tag{2.2}$$

Here, $\rho_0$, $d_0$, and $\psi$ are the mean density of center of mass, smectic layer spacing, and smectic order parameter, respectively. The smectic order parameter $\psi$ is the ratio of the amplitude of oscillation to the mean layer density, and hence expresses the extent to which the material is layered. Inside the layers of SmA phase, molecules can move like in liquids and there is no correlation in the position among them in adjacent layers. Smectic layers are flexible and slide over each other. Uniformity of the layers can be easily distorted by the interlayer spacing tends to be preserved. As show in Fig. 2.2(b), SmA phase is optically uniaxial similarly to the nematic phase.

Now, let the SmC phase described in Fig. 2.2(c) be introduced. Similarly to the SmA phase described above, molecules in SmC phase are still arranged in layers. However, they are not free to rotate around their long axis. The long axes of molecules are tilted in a preferred direction with respect to the layer normal. The tilt direction of the molecules in neighboring layer is strongly correlated. Thus, the projections of the molecules in the plane of the layers are aligned in a common direction. This is usually denoted by a unit vector **c**. The system remains invariant for the transformation in direction **n** to – **n** but not

for the **c** director. The angle between the director **n** and the normal vector of layers **k** defines the tilt angle of the materials. The fact that the molecules tilt away from the layers means that the director is confined to a conical surface of which the normal vector of layers is the axis. Therefore, the movement of the director is very limited to the orientations defined in space by the smectic cone.

If chiral molecules are mixed with achiral molecules in the SmC phase, the ferroelectric SmC* phase in Fig. 2.2(d) is formed. This phase was deduced from symmetry considerations that all chiral tilted smectic phases exhibit a spontaneous polarization $P_s$, and thus show pyroelectricity. The spontaneous polarization $P_s$ is defined as [8]

$$P_s = P_0(\mathbf{k} \times \mathbf{n}) \tag{2.3}$$

where $P_0$ is the linear tilt-polarization coupling constant. In the case where this spontaneous polarization can be reoriented between two stable states by application of an electric field, so-called ferroelectricity. In fact, the bulk SmC* phase doesn't show this behavior, because in the field-free state, it exhibits a helical superstructure, such that the spontaneous polarization vanished over the distance of the pitch. The SmC* phase is thus more correctly called helielectric. Nevertheless, this phase has attracted much interest not only due to its interesting fundamental physics, but also due to its promising properties for applications in fast switching, high contrast, and large viewing angle display, and other non-display applications. This was triggered by the field of FLCs, the discovery of the surface stabilized FLC (SSFLC) state. This led to extensive investigations of SmC* materials.

### 2.1.3. Alignment of Liquid Crystals

The surface alignment of LCs is very important for a basic understanding of interfacial interactions between LC molecules and solid substrates as well as for practical electro-optical applications. It is generally believed that anisotropic surface interactions in addition to geometrical surface patterns of the substrates dictate the LC alignment. In this section, several LC alignment techniques and some LC orientational geometries are briefly introduced.

There are two typical principles of alignment of LC as shown in Fig. 2.3. One is the mechanically induced alignment which determines the direction of LC molecules by the direction of nano- or micro-scaled grooves. Since the typical LC molecules have rod-like shape, they tend to be aligned along the direction of the groove as shown in Fig. 2.3(a). This tendency grows stronger as the amplitude of grooved structures increases and the period of grooved structure decreases. The other alignment mechanism is the chemically induced alignment. In this mechanism, the direction of LC molecule is determined by the van der Waals interaction between the LC molecule and the side chain of the alignment material as shown in Fig. 2.3(b). In order to achieve stable alignment of LC molecules, polymer materials having proper side chains are commonly used as alignment materials. The direction of the period of the side chain can be controlled by the physical contacts or the incident electromagnetic waves. It should be noted that Fig. 2.3(a)-(b) are just examples of mechanically and chemically induced alignment of LC, and the

alignment geometry of LC is different according to the types of alignment materials or the physical structure of the surface.

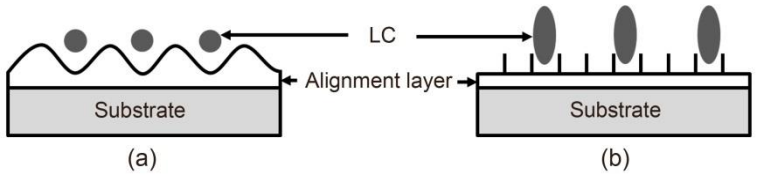


**Figure 2.3.** (a) Mechanically induced and (b) chemically induced alignment of LC.

Figure 2.4 shows three typical LC alignment techniques. The most widely used LC alignment technique is rubbing technique depicted in Fig. 2.4(a). The rubbing is still the most dominant alignment process, which means that rubbing an organic polymer coated substrate using a rotating drum covered by a cloth with short fibers. Although this process has many problems such as generation of dust and static electricity, many LC-based devices cannot be fabricated without it since it needs a short and simple process and can be applied to a large area at low cost. The rubbing controls both azimuthal and polar angles of the LC alignment. The alignment materials also affect the quality of the LC alignment. In the past, polyvinyl alcohol, acrylic polymers, and vinyl polymers were tested as an alignment material, and finally, polyimide (PI) has been used most widely. The reason why PI became the dominant alignment material is its stability and superior electric properties. In the case of device driven by thin film transistors, the electric properties are as important as the alignment quality. Although there are many reports analyzing

mechanism of the rubbing, there are still a lot of controversies related to the exact principle of LC alignment on the rubbed solid substrate.

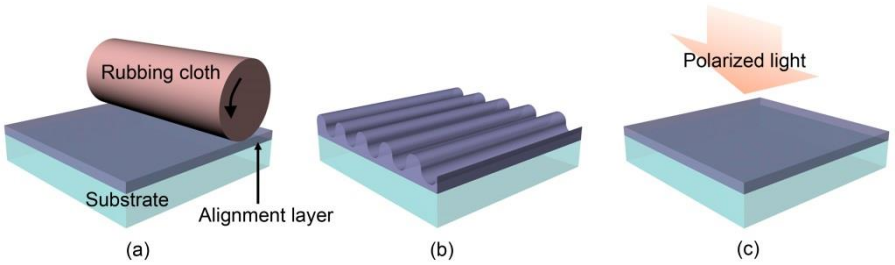


**Figure 2.4.** Schematic illustration of (a) rubbing alignment, (b) alignment on the microgroove structure, and (c) photoalignment of LC.

Figure 2.4(b) depicts the LC alignment on microgrooves. The microgroove structure itself can cause LC materials to align in the direction parallel to the groove structure. Several processes to produce surfaces with microgroove structures for LC alignment has been proposed, for example, reactive ion-etching on glass substrates with chromium masks, photolithographic technique for photoreactive polymers using holographic exposure and reactive etching on the $SiO_2$ surface, pressing on of the microgroove surface fabricated by the holographic light exposure, and the exposure of ultraviolet (UV) light onto photocurable polymer film through masks with grating patterns. In all cases, it has been reported that microgrooves with a pitch smaller than 1 μm can realize an LC alignment giving a practical contrast. This alignment property of microgroove is also

known as Berreman effect, and the azimuthal anchoring energy on the microgroove surface $W_e$ and the shape of microgroove have relation of [9]

$$W_e \propto \frac{\pi^3 k A^2}{2B^3} \tag{2.4}$$

where $k$, $A$, and $B$ are the isotropic elastic constant of LC, the amplitude of the microgroove, and the period of microgroove, respectively.

Figure 2.4(c) depicts the photoalignment technique of the LC. Photoalignment technique is a simple alignment technique which uses a polarized light. The alignment direction of LC molecules is determined by exposing linearly polarized light to the photo-responsive alignment layer. This method has been realized by using UV exposed azobenzene-mixed PI at first, and special photochemical reactions such as dimerization or isomerization were used and only a few limited types of photoalignment materials were involved. After it was found that PI exposed to linearly polarized deep UV light showed LC alignment, a wider variety of materials have been able to be used for photoalignment. A viewing angle improvement was a big issue for LC display (LCD) manufacturers in 1990s, and the multiple domain technique induced by photoalignment was developed to enhance the viewing angle. Since the need for multiple domains in LCDs reduced by the appearance of various LCD modes and optical compensate films, the need for photoalignment also reduced. However, recent trends towards larger display panel sized and higher resolutions, and the advent of more display modes have increasingly exposed the limitations of the rubbing process. The desire for a new and improved alignment technology steadily became stronger, and

today, many types of photoalignment have been developed, and the choices of materials have increased. Nowadays, all ranges of pretilt angles can be established by photoalignment, and not only linearly polarized light, but also a non-polarized light can be used as the light source for photoalignment.

By aligning LC molecules in particular directions with various pretilt angles through alignment techniques described above, diverse LC cell geometries can be obtained as shown in Fig. 2.5. Since LC-based devices usually employ superb optically anisotropic characteristics, most devices are fabricated by injecting LC into the space between two substrates coated by alignment materials. These LC geometries are classified into two groups. The directors of the LC molecules in the homogeneous, tilted, and homeotropic cases are aligned in one fixed direction while the director of the LC molecules in the hybrid, splay, twisted, and bend are not fixed in one direction. In the latter geometries, LCs are under stress. LC molecules are aligned parallel to the substrates in the homogeneous and perpendicular to the substrates in the homeotropic alignments. Tilted alignment is an intermediate state between homogeneous and homeotropic, and the LC molecules are tilted at a certain pretilt angle. Actually, the tilted alignment with low pretilt angle ($\leq 10°$) is often called homogeneous. In the hybrid alignment, LC molecules on one substrate have homogeneous alignment and those on the other substrate have homeotropic alignment. Homeotropic alignment had been obtained by substrates coated with hydrophobic films, however nowadays, PI films with hydrophobic side chains are used widely for obtaining homeotropic alignment.

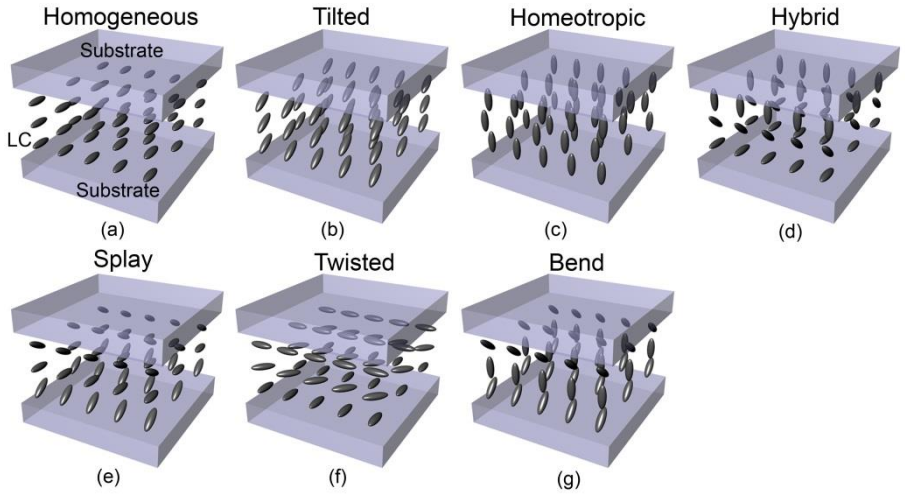


**Figure 2.5.** Schematic illustration of (a) homogeneous, (b) tilted, (c) homeotropic, (d) hybrid, (e) splay, (f) twisted, and (g) bend geometries of LC.

The LC molecules near the substrate affect the LC orientation in the bulk by molecular-molecular interactions, and the orientation in the entire LC cells is determined. In most cases, the interaction between the substrates and the LC molecules near the surface is very strong. By the application of electric or magnetic fields, the alignment of LC near the substrate is hardly changed. Such a relationship between the substrate surface and the LC is called strong anchoring. In case of the strong anchoring having strong anchoring energy *W*, after removing the electric or magnetic field, the LC orientation recovers to that of the initial orientation. In contrast, when the LC orientation after removing the field is different from the initial orientation, the relationship is called weak anchoring.

## 2.2. Reorientation of Liquid Crystals

The LC molecules aligned on surfaces can be reoriented by external stimuli such as electric field and light. This provides dynamic characteristics of the LC-based electro-optical device, and the surface properties are involved in the LC reorientation process. Therefore, the structured order can be produced through the LC reorientation by the spatially varying surface properties as well as the spatially varying external fields. In this section, the electric field-induced and light-induced LC reorientation processes for producing the structured order of the LC molecules are introduced.

### 2.2.1. Electric Field-Induced Reorientation

LC molecules under the external electric field are reoriented by an electric torque due to their dielectric anisotropy described above briefly. If an electric field is applied to the NLC, a rotational torque is generated by the coupling between the electric field **E** and the electric displacement **D**, and it can be expressed as

$$\mathbf{D} = \varepsilon_{\perp}\mathbf{E} + (\varepsilon_{\parallel} - \varepsilon_{\perp})(\mathbf{n}\cdot\mathbf{E})\mathbf{n} \,. \tag{2.5}$$

Here, ε is the static dielectric constant, measured along ($\varepsilon_{\parallel}$) or normal ($\varepsilon_{\perp}$) to the LC director **n** with unity length. Then, the electrostatic energy density contributing to the thermodynamic potential is

$$f_{\text{elec}} = -\frac{1}{2}\mathbf{D}\cdot\mathbf{E} = -\frac{1}{2}\Delta\varepsilon(\mathbf{n}\cdot\mathbf{E})^2 - \frac{1}{2}\varepsilon_{\perp}\mathbf{E}^2, \tag{2.6}$$

where the dielectric anisotropy $\Delta\varepsilon = \varepsilon_{\parallel} - \varepsilon_{\perp}$. For $\Delta\varepsilon > 0$, the LC molecules tend to be reoriented parallel to the electric field to lower electrostatic energy. On the contrary, the LC molecules are reoriented perpendicularly to the electric field under the condition of $\Delta\varepsilon < 0$.

The LC directors of the averaged orientation of the LC molecules are determined from the elastic continuum theory based on the deformation energies. Due to the curvature elasticity of LCs, the LC reorientation is balanced between the electric torque and the elastic restoring torque that determines the static deformation of LC molecules. In the NLC phase, where the cylindrical symmetry of the structure as well as the absence of the polarity must be taken into account, there are three basic types of the deformations: splay, twist, and bend distortions. In such symmetries, the Frank-Oseen elastic free energy for the NLC is expressed as [10,11]

$$f_{\text{elas}} = \frac{1}{2}K_1(\nabla\cdot\mathbf{n})^2 + \frac{1}{2}K_2(\mathbf{n}\cdot\nabla\times\mathbf{n})^2 + \frac{1}{2}K_3(\mathbf{n}\times\nabla\times\mathbf{n})^2, \tag{2.7}$$

where $K_1$, $K_2$, and $K_3$ are the elastic coefficients corresponding to the splay, twist, and bend deformations, respectively. The total bulk free energy density $f$ is obtained by the summation of two energy densities, $f_{\text{elec}} + f_{\text{elas}}$.

Under the finite surface anchoring, the surface anchoring energy density is obtained as [12]

$$F_{\text{surf}} = \frac{1}{2}W_{\text{p}}(\theta-\theta_{\text{p}})^2 + \frac{1}{2}W_{\text{a}}(\phi-\phi_{\text{a}})^2. \tag{2.8}$$

Here, $W_p$ and $W_a$ denote the polar anchoring strength and the azimuthal anchoring strength, respectively. θ and ϕ are tilt angle of the LC director from the substrate normal and the azimuthal angle of the LC director from the easy axis, respectively, as shown in Fig. 2.6. The easy axes of LC mean the intrinsic alignment directions in polar and azimuthal directions and are represented by $\theta_p$ and $\phi_a$, respectively. Based on these equations, LC molecules have their own alignment direction under the certain applied electric field and the anchoring energy on the substrates in order to minimize the total free energy

$$F_{total} = \iiint f_{elec} + f_{elas} dxdydz + \iint F_{surf} dxdy . \quad (2.9)$$

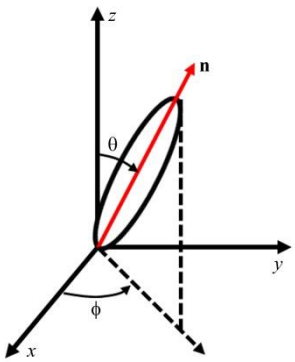


**Figure 2.6.** The coordinate system for the LC director **n**. Here, ϕ is the azimuthal angle from the *x*-axis and θ is molecular tilt angle out of *x*-*y* plane.

## 2.2.2. Light-Induced Reorientation

In all-optical devices, the light controls the polarization state or the phase of the light with the help of a nonlinear optical material. Nonlinear optical effects can be direct or indirect. Direct effects occur at the atomic or molecular level when the presence of the light alters the atomic susceptibility or the photon absorption rates of the medium. The optical Kerr effect and the saturable absorption are examples of direct nonlinear optical effects. Indirect nonlinear optical effect involves an intermediate process such as photorefractivity in which charge carriers photogenerated by the nonuniform illumination redistribute over macroscopic distances and the resultant space-charge electric fields modify the optical properties of the medium. Since the LC is an nonlinear optical material having superb electrical and/or optical anisotropy, the LC or liquid crystalline mixtures has been widely studied as a photoresponsive medium.

There are two typical types of photomodulation of orientation of LC molecules [13]: change in LC director and change in phases. In both cases, a large change of in refractive index can be induced. When LC molecules are aligned vertically, linearly polarized light with its electric vector oscillating in the vertical direction detects an extraordinary refractive index $n_e$. If the alignment of LC molecules is changed from the vertical to the horizontal state with actinic light as a stimulus, the linearly polarized light will detect an ordinary refractive index $n_o$. This means that a change in refractive index is induced, which corresponds to the value of $\Delta n = n_e - n_o$. A phase transition gives rise to a change in refractive index, $n_e - n_{iso}$, where $n_{iso}$ is the refractive index of an isotropic phase. The order of the refractive index is usually $n_e >$

$n_{iso} > n_o$, thus the change in the director gives rise to a larger change in the refractive index. In this section, the basic principle of the photomodulation of LC orientation by phase transition is introduced.

For the dynamic photomodulation of LC molecules, the guest/host systems which mean the mixture of LC and dye are used most widely. When a small amount of photochromic molecules such as azobenzenes, stilbenes, spiropyrans and fulgides are incorporated into LC molecules and the resulting guest/host mixtures are irradiated to cause photochemical reactions of the photochromic guest molecules, an LC to isotropic phase transition of the mixture can be induced isothermally. For example, azobenzene with rod-like *trans* form stabilizes the phase structure, while its isomer with bent *cis* form tends to destabilize the phase structure of the mixture as shown in Fig. 2.7(a). As a result, the nematic-isotropic phase transition temperature ($T_c$) of LC mixed with *cis*-form azobenzene molecules ($T_{cc}$) is lower than that of the LC mixed with *trans*-from azobenzene molecules ($T_{ct}$) as shown in Fig. 2.7(b). Therefore, if the temperature of the sample ($T$) is set at a temperature between $T_{cc}$ and $T_{ct}$, and the sample is irradiated to cause *trans-cis* isomerization of azobenzene molecules, the nematic-isotropic phase transition of the sample is induced. These photochromic reactions are usually reversible. However, the gap between $T_{cc}$ and $T_{ct}$ is usually not broad, and when the temperature of the sample is set below $T_{cc}$, no phase transition is induced even upon the prolonged irradiation. There have been many researches and studies based on these basic principle of photoreaction using LC and dye mixture. Since the

*trans-cis* isomerization occurs at most dyes having azo-compound, numerous azo-dye and NLC mixtures have been studied.

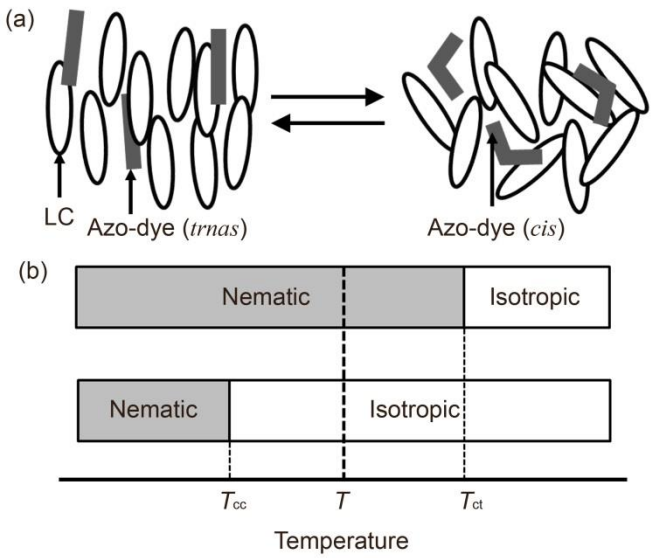


**Figure 2.7.** (a) Phase diagram of the photochemical phase transition of azobenzene/LC system and (b) the change of isotropic-nematic phase transition temperature.

# Chapter 3. Fully Continuous Liquid Crystal Grating

## 3.1. Introduction

LCs are widely used for optical devices due to the large electro-optic modulation resulting from the high optical anisotropy, the electrically tuning capability at low voltages, and the design flexibility on various substrates [14-19]. Among a number of the LC devices, the LC grating elements play an important role in many optical systems such as 3D displays, optical data storage, and optical communication systems by means of the change in the phase or the polarization state of light [15,20-24]. Although the LC grating devices with simple binary patterns have been commonly used [25-28], more sophisticated gratings including step-wise discrete gratings and continuous gratings are needed for specific applications [19,29-35]. The step-wise LC gratings fabricated using a micro-rubbing method [24,34] or a micro-electrode patterning method [35] suffer from the discontinuity of the phase retardation due to the uniform alignment of the LC molecules within each step-wise pattern in alternating domains. On the other hand, a rather continuous version of the LC grating obtained through photoalignment of the LC using holographic methods [19,29-33], shown in Fig. 3.1(a), is capable of eliminating higher-orders of diffraction except for ±1st orders whose

polarization states are circular. This type always involves the disclination in the LC alignment from one domain to the other and thus possesses the mirror symmetry. The resultant diffraction properties were found to depend on the thickness of the LC cell. Therefore, it is very important to understand the diffraction properties of the continuous LC gratings in term of the symmetry argument from the fundamental as well as practical viewpoints regardless of their diffraction efficiencies.

In this chapter, a fully continuous LC grating device with the rotational symmetry of the LC alignment which exhibits the switching effect between the diffraction orders independent of the thickness of the LC cell is demonstrated. A simple and low-cost imprinting technique [36] was employed to produce the alternating semi-circular alignment of the LC as shown in Fig. 3.1(b). It was found that the LC molecules were well aligned along the direction of the microgrooves defined by the imprinting process due to the Berreman effect [9,37]. This LC grating showed the perfect continuity of the phase retardation and the switchable diffraction with the diffraction efficiency of 44% at ±1st orders. Due to the rotational symmetry, two symmetric grating configurations were produced depending on the input polarization direction with respect to the grating patterns. The experimental results were found to agree well with the theoretical predictions made in the transfer matrix formalism.

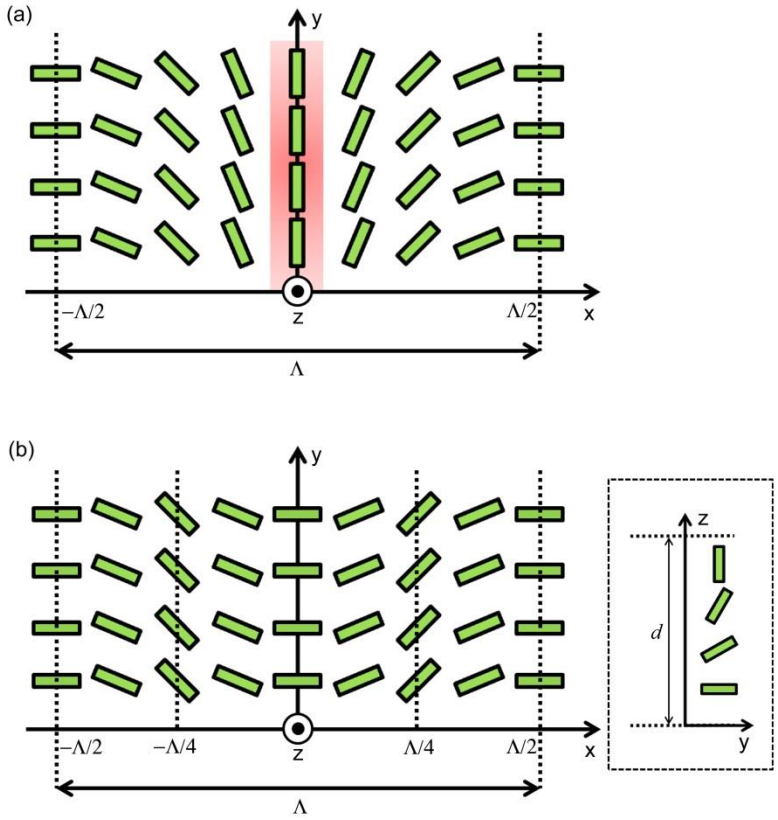


**Figure 3.1.** Schematic representation of the distribution of the LC director in (a) a continuous grating structure with a wall (indicated in red) separating two domains and (b) a fully continuous grating structure with no wall in alternating semi-circular (quadrant) forms and the LC director in *y*-*z* plane. The green bars represent the LC molecules. (Ref. [3])

## 3.2. Transfer Matrix Formalism for Diffraction

Consider the distribution of the LC director on the bottom substrate in one period of a continuous LC grating shown in Fig. 3.1(b). In the hybrid LC geometry used in this study, a schematic diagram of the LC director in the *y*-*z* plane was shown in the right of Fig. 3.1(b). Here, the LC molecules are aligned in alternating semi-circular (quadrant) forms and the director of LC molecules is then written as

$$n(x) = [\cos(\pi x / \Lambda), \sin(\pi x / \Lambda), 0], \tag{3.1}$$

for $-\Lambda/4 \leq x < \Lambda/4$. For $-\Lambda/2 \leq x < -\Lambda/4$ or $\Lambda/4 \leq x < \Lambda/2$, the LC director is given as

$$n(x) = [\sin(\pi x / \Lambda), \cos(\pi x / \Lambda), 0]. \tag{3.2}$$

Here, $\Lambda$ means the period of the LC alignment patterns. In this configuration, the LC director (or the phase retardation) changes in an alternating semi-circular (quadrant) form along the *x*-axis.

The electric field $D_m$ of the output beam through the diffraction grating device at the diffracted order *m* can be expressed as

$$D_m = \frac{1}{\Lambda} \int_{-\Lambda/2}^{\Lambda/2} T(x) \exp(-2m\pi x i / \Lambda) E_{in} dx, \tag{3.3}$$

where $T(x)$ denotes 2 × 2 Jones transfer matrix and $E_{\text{in}}$ is the Jones vector of the input beam. Assuming that the LC molecules are uniform along the *y*-axis and ignoring the absolute phase change, the transfer matrix $T(x)$ can be simplified as

$$T(x) = \cos(\Delta n d\pi / \lambda) \begin{bmatrix} 1 & 0 \\ 0 & 1 \end{bmatrix} + i \sin(\Delta n d\pi / \lambda) \begin{bmatrix} -\cos(2\pi x / \Lambda) & -\sin(2\pi x / \Lambda) \\ -\sin(2\pi x / \Lambda) & \cos(2\pi x / \Lambda) \end{bmatrix}, \tag{3.4}$$

for $-\Lambda/4 \leq x < \Lambda/4$. For $-\Lambda/2 \leq x < -\Lambda/4$ or $\Lambda/4 \leq x < \Lambda/2$, the transfer matrix $T(x)$ is written as

$$T(x) = \cos(\Delta n d\pi/\lambda)\begin{bmatrix} 1 & 0 \\ 0 & 1 \end{bmatrix} + i\sin(\Delta n d\pi/\lambda)\begin{bmatrix} \cos(2\pi x/\Lambda) & -\sin(2\pi x/\Lambda) \\ -\sin(2\pi x/\Lambda) & -\cos(2\pi x/\Lambda) \end{bmatrix}. \tag{3.5}$$

Here, $\Delta n$ is the birefringence of the LC, $d$ is the thickness of the LC layer, and $\lambda$ is the wavelength of the input beam. The two domains in Fig. 3.1(a), represented by Eq. (3.1) and Eq. (3.2), were used in the previous works using the photoalignment method [19,29-31,33]. Note that the disclination in the LC alignment between two adjacent domains exists in Fig. 3.1(a) while the continuous symmetry with no wall is shown in Fig. 3.1(b).

Let the electric fields of the output beam at several low orders of diffraction from Eqs. (3.3)-(3.5) in the hybrid alignment geometry which has the rotational symmetry with respect to the substrate normal be calculated. From the fact that under no applied voltage in the hybrid geometry, the phase retardation along the easy axis is $\lambda/2$ regardless of the thickness of LC layer, the values of $\cos(\Delta n d\pi/\lambda)$ and $\sin(\Delta n d\pi/\lambda)$ are 0, 1, respectively, in Eqs. (3.4) and (3.5). As a result, the electric fields at the diffraction orders of 0th, ±1st, and ±2nd are calculated as

$$D_0 = \frac{2}{\pi} i \begin{bmatrix} -1 & 0 \\ 0 & 1 \end{bmatrix} E_{in}, \tag{3.6}$$

$$D_{\pm 1} = \frac{1}{2} \begin{bmatrix} 0 & \mp 1 \\ \mp 1 & 0 \end{bmatrix} E_{in}, \tag{3.7}$$

$$D_{\pm 2} = \frac{2}{3\pi} i \begin{bmatrix} \mp 1 & 0 \\ 0 & \pm 1 \end{bmatrix} E_{in} . \quad (3.8)$$

It should be noted that the diffracted intensities at higher orders than ±2nd are negligibly small. Using Eqs. (3.6)-(3.8), the diffraction efficiencies at 0th, ±1st, and ±2nd orders are calculated as 40.5%, 50%, and 9%, respectively. In the presence of an applied voltage, the magnitude of the phase retardation itself changes, but the switching phenomenon among the diffraction orders is independent of the LC cell thickness.

## 3.3. Fabrication Process of Diffraction Grating

Figure 3.2(a) depicts the schematic diagram of the LC grating cell with the fully continuous, alternating semi-circular alignment of the LC. The fabrication process of the bottom substrate with alternating quadrant patterns by imprinting was shown in Fig. 3.2(b). A photo-curable polymer (NOA65; Norland) was first prepared on an indium-tin-oxide (ITO) coated glass substrate by spin coating at the rate of 2000 rpm for 30 s. The substrate was then imprinted with a master mold which was fabricated with poly(dimethylsiloxane) (PDMS; Dow Corning). The master mold had alternating quadrant patterns with a period of 60 μm. The imprinted substrate together with the master mold was exposed to UV light at the intensity of 100 mW/cm$^2$ for 10 min. The master mold was finally peeled-off. The top substrate in Fig. 3.2(a) was made of an ITO coated glass substrate on which the vertical alignment layer of PI (AL00010; JSR) was prepared by spin

coating at the rate of 3000 rpm for 30 s. The alignment layer was baked at 180 ℃ for 90 min. The thickness of the LC cell was maintained using glass spacers of 9.5 μm thick and a NLC (ZLI-2293, $\Delta n$ = 0.13, $\Delta\varepsilon$ = 10; Merck) was injected into the cell by capillary action at room temperature.

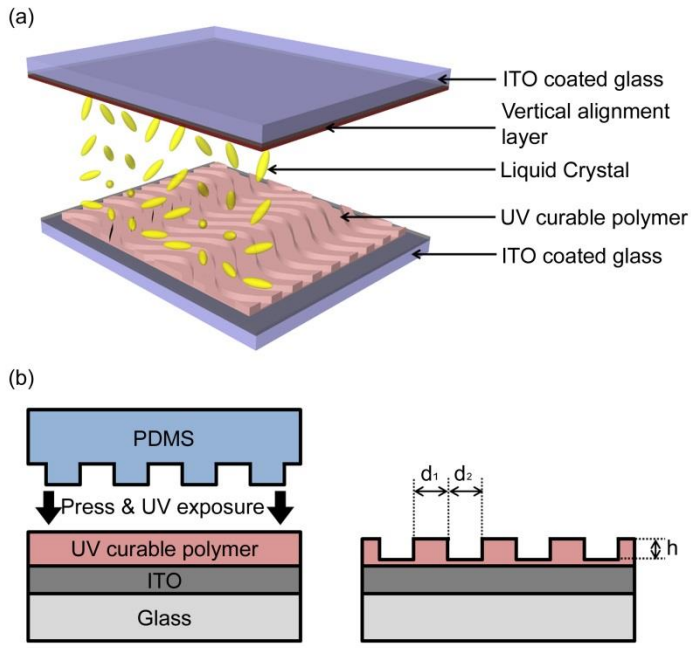


**Figure 3.2.** (a) Schematic diagram of the LC grating cell and (b) the fabrication process of the bottom substrate with sinusoidal patterns by imprinting ($d_1$ = $d_2$ = 3 μm, and $h$ = 1 μm). (Ref. [3])

Figures 3.3(a) and 3.3(b) show the optical microscopic image of the alternating semi-circular patterns on the bottom substrate and the image of the microgrooves observed with a scanning electron microscopy (SEM;

XL30FEG, Phillips), respectively. The height of each microgroove was about 1 μm and the separation between two adjacent microgrooves was 3 μm.

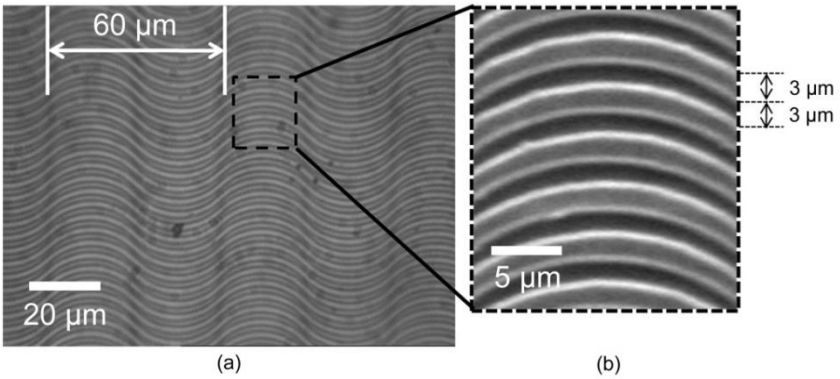


**Figure 3.3.** (a) The optical microscopic image of alternating semi-circular patterns on the bottom substrate. (b) The SEM image of the microgrooves in the semi-circular patterns on the bottom substrate. (Ref. [3])

Figures 3.4(a), 3.4(b), and 3.4(c) show optical microscopic textures (Optiphot2-Pol; Nikon) toher with the LC distortions in this continuous LC grating device under parallel polarizers in the presence of the applied voltage of (a) 0, (b) 25, and (c) 100 V, respectively. Under no applied voltage, the LC molecules were aligned along the microgrooves defined by imprinting on the bottom substrate and vertically on the top substrate as shown in Fig. 3.4(a). Depending on the angle between the easy axis (or optic axis) and the polarizer, the transmitted light intensity is continuously modulated within each domain as seen in Fig. 3.4(a). As the applied voltage increases, the LC molecules in the bulk are reoriented along the electric field direction and the grating effect

from the alternating semi-circular alignment on the bottom substrate becomes to diminish as shown in Fig. 3.4(b). At 100 V, the grating patterns almost disappear as shown in Fig. 3.4(c). It is noted that due to the relatively large feature size (3 μm) of the microgrooves, the static background patterns were seen in Fig. 3.4 and the LC molecules would be less aligned.

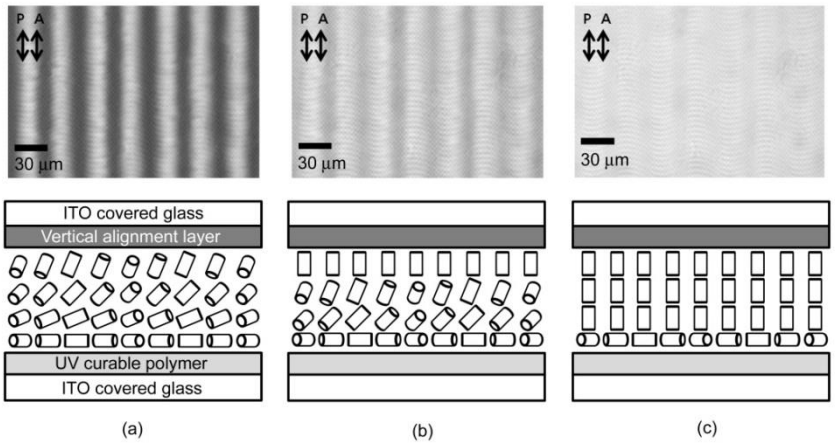


**Figure 3.4.** Optical microscopic textures together with the LC distortions in the continuous LC grating device under parallel polarizers in the presence of the applied voltage of (a) 0, (b) 25, and (c) 100 V. (Ref. [3])

## 3.4. Result and Discussion

### 3.4.1. Polarization-Dependent Diffraction Properties

Let the diffraction properties of the fully continuous LC grating device be examined as a function of the applied voltage. Measurements were carried out

using a He-Ne laser with the wavelength $\lambda$ = 632.8 nm as a light source in conjunction with a charge-coupled device and a photodetector. The input beam was linearly polarized and the input polarization direction with respect to the grating patterns was set to be 90° or 45°. Figure 3.5(a) shows the experimental geometry for measuring the diffraction patterns in the input polarization direction of 90°. The diffracted patterns under no analyzer, a crossed analyzer, and a parallel analyzer are shown in Figs. 3.5(b), 3.5(c), and 3.5(d), respectively. As clearly seen in Fig. 3.5(b), the diffraction orders of 0th and ±1st are dominant under no analyzer and the orders higher than ±2nd are negligible. Under a crossed analyzer, ±1st (odd) orders of diffraction are essentially observed as shown in Fig. 3.5(c) while under a parallel polarizer, the 0th and the ±2nd (even) orders are appeared as in Fig. 3.5(d). This indicates that 0th and ±2nd orders maintain the input polarization state while ±1st orders change it by 90°.

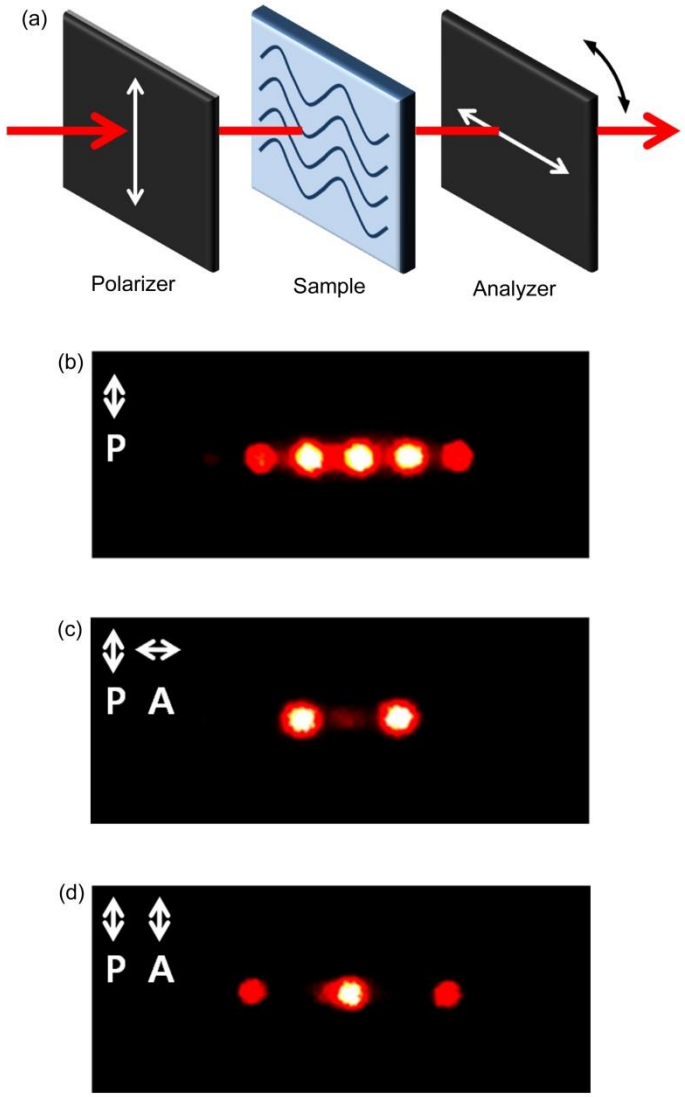


**Figure 3.5.** Experimental geometry for measuring the diffracted patterns in the input polarization direction of 90°. The diffraction patterns under (b) no analyzer, (c) a crossed analyzer, and (d) a parallel analyzer. (Ref. [3])

Figure 3.6(a) shows the experimental geometry for measuring the diffraction patterns in the input polarization direction of to 45° with respect to the grating patterns. The diffraction patterns under no analyzer, a crossed analyzer, and a parallel analyzer are shown in Figs. 3.6(b), 3.6(c), and 3.6(d), respectively. It should be noted that under no analyzer, the diffraction orders observed are exactly the same as those for the case in the input polarization direction of 90°. Moreover, from Figs. 3.5(c), 3.5(d), 3.6(c), and 3.6(d), it was found that the rotation of the input polarization with respect to the grating patterns by 45° corresponds to the interchange between the crossed configuration and the parallel configuration. In other words, for the case of the input polarization direction of 45°, the polarization states of $\pm$1st orders remain unchanged while those of 0th and $\pm$2nd orders are rotated by 90°. Such diffraction properties can be well described from Eqs. (3.6)-(3.8) where the geometric symmetry of the LC alignment in this LC grating is reflected. The non-vanishing diffracted intensity at 0th order in Fig. 3.5(c) or Fig. 3.6(d) may be attributed to the static background microgroove patterns and the LC alignment quality that originate solely from the microgroove pattern features but not from the intrinsic symmetry of the LC grating structure.

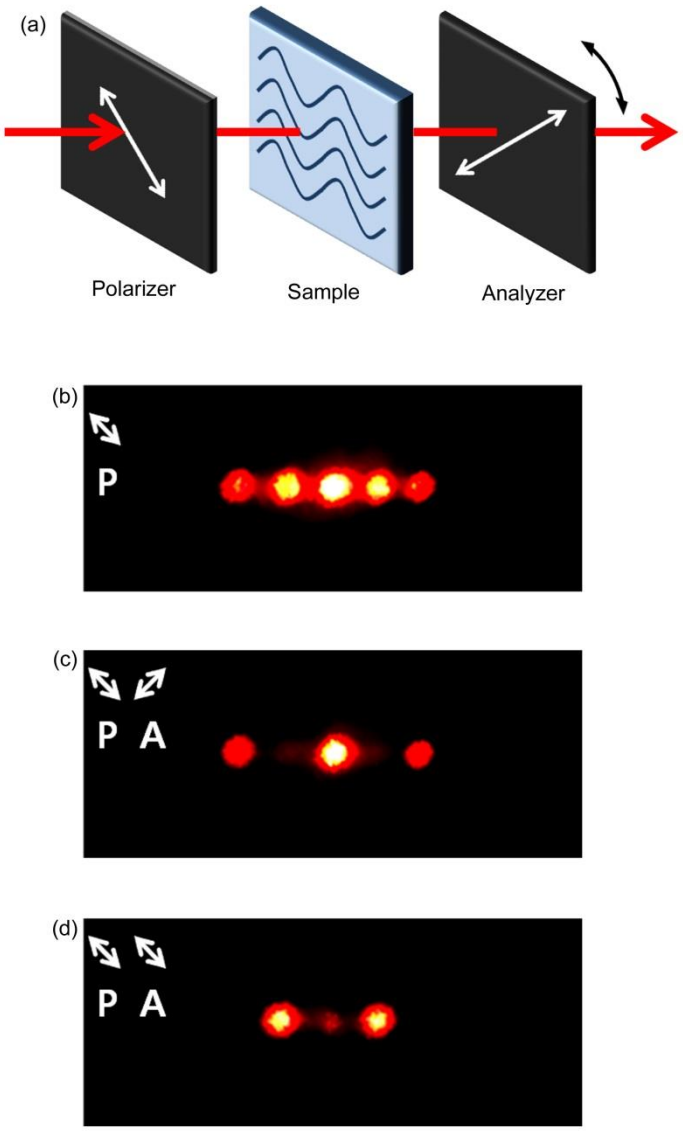


**Figure 3.6.** Experimental geometry for measuring the diffracted patterns in the input polarization direction of 45°. The diffraction patterns under (b) no analyzer, (c) a crossed analyzer, and (d) a parallel analyzer. (Ref. [3])

### 3.4.2. Electrically Tunable Diffraction Properties

The switching effect between the diffraction orders as a function of the applied voltage is described now. Figures 3.7(a) and 3.7(b) show the diffracted patterns at the applied voltages of 0 and 100 V, respectively. Under no applied voltage, there exists ±1st orders of diffraction while at a high applied voltage of 100 V, only 0th order appears. It is noted that the diffraction orders observed in the transverse-periodic structure [30] are appeared either positive or negative orders depending on the input polarization. In contrast, in this LC grating structure with high symmetry, both positive and negative orders of diffraction are always produced irrespective of the input polarization. The measured diffraction efficiency at ±1st orders was found to be about 44% which is somewhat less than the theoretical value (50%) calculated from Eq. (3.7). In fact, the anchoring energy on the homeotropic surface (the top substrate) plays an important role on the diffraction efficiency. However, in this case, the anchoring energy of the homogeneous, bottom substrate influences the diffraction properties more strongly since the anchoring strength achieved by the grooves of about 3 μm is relatively weak compared to the homeotropic case. In addition, the incidental defects involved in the LC alignment contribute to the difference. The voltage-dependent switching effect between the diffraction orders of 0th and ±1st is shown in Fig. 3.7(c). At about 15 V, the three diffracted intensities are nearly identical. On further increasing the applied voltage above 15 V, the diffracted intensity at ±1st order decreases and eventually vanishes while those at 0th orders increase and

become saturated. Note that the driving voltage, being somewhat high, can be simply reduced with decreasing the voltage drop across the imprinted alignment layer, meaning that the thinner the imprinted alignment layer is, the lower the driving voltage is. The switchable features of this LC grating device will be useful for separating an original image into two different types of diffractive images.

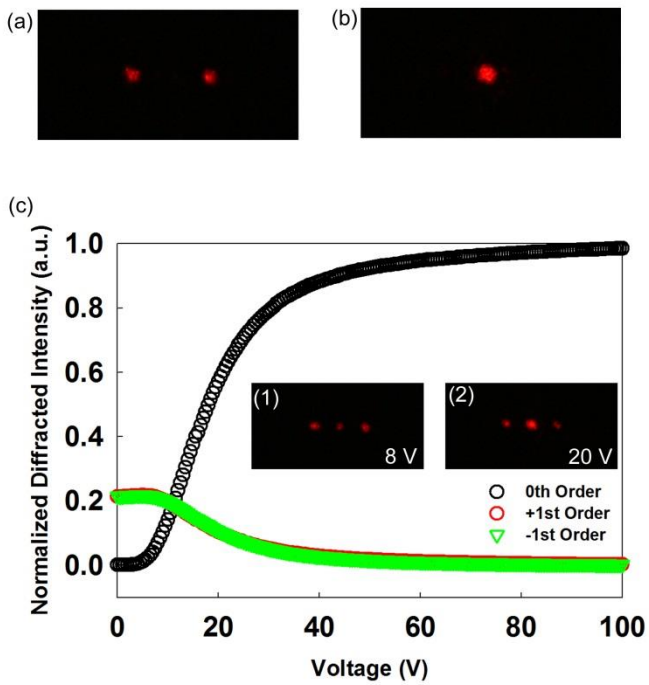


**Figure 3.7**. Diffracted patterns under a parallel analyzer in the input polarization direction of 45° at (a) 0 V and (b) 100 V. (c) The normalized intensities at 0th and ±1st orders as a function of the applied voltage. The inset in (c) show the diffraction patterns at 8V and 20 V. (Ref. [3])

## 3.5. Summary

A new type of the LC grating device possessing the continuously graded phase retardation within an individual grating pattern was demonstrated. The fully continuous phase retardation was achieved using the semi-circular alignment of the LC on a microgrooved substrate fabricated through an imprinting process. The continuous LC grating with rotation symmetry exhibited the switching effect between the diffraction orders of 0th and ±1st. The diffraction efficiency at ±1st orders was found to be about of 44%. The continuous grating architecture with high symmetry presented here will be applicable for devising a variety of optical elements including a tunable beam splitter and a switchable diffractive component.

# Chapter 4. Optically Switchable Ferroelectric Liquid Crystal Grating

## 4.1. Introduction

In recent years, various types of optically activated photonic devices such as optically tunable gratings [13,38-45], microlenses [46,47], optical filters [48,49], optical switches [50,51], optical memories [13,27], and photonic crystals [52] have been paid much attention due to a wide range of applications in optically addressed systems from information processing to bio-sensing [41]. Among them, optical gratings are considered as essential components for optical routing, data storage, and 3D displays [27]. Optically tunable diffraction gratings have been fabricated typically using dye-doped LCs [13,38-42] owing to the wide tuning capability of the optical properties resulting from the large change of the optical and/or electro-optical anisotropy under small external perturbations, the self-organizing nature, and the fluidity with long-range order [13,40]. Particularly, in the case that the LC is doped with the dye molecules that undergo reversible *trans-cis* isomerization by the exposure of light at a particular wavelength for absorption, the photo-isomerization of the dye tends to disturb the neighboring LC alignment [13,38-41]. This results in the change of the nematic-isotropic phase transition temperature $T_c$ as revealed in azo-dye-doped NLCs previously [13]. Within the framework of the phase transition between $T_c$ for the *trans*-case and $T_c$ for

the *cis*-case by the pump beam, a variety of optically switchable gratings and waveguides have been demonstrated [38-42,53]. However, the change of $T_c$ is usually small and the amount of the change in the optical modulation is negligibly small except for the vicinity of $T_c$. In other words, even upon the prolonged irradiation of a strong pump beam, no significant change in the optical modulation can be achieved at temperatures away from $T_c$ regardless of the *trans-cis* transformation of the dye molecules [13,54]. Moreover, the optical modulation resulting from the collective rotation of the LC molecules takes place in several seconds to tens of minutes in the orientationally ordered (nematic) state [13,38-42,48-51]. The photo-induced switching of the LC is known to be quite slow compared to other types of switching driven by the application of an electric field [55] or pressure [56]. From the viewpoint of the optical and/or electro-optic response, FLCs are promising owing to the spontaneous polarization and the layered order in addition to the orientational order. However, no comprehensive picture of all-optical switching in the grating configuration has not been obtained so far although azo-dye-doped FLCs have been extensively studied for the photo-induced phase transitions and the photochemical switching of the polarization [53,57-61]. Note that for the FLCs, one of the critical issues is to achieve the uniform and stable alignment of the molecules in layers [62,63], particularly, in the device architecture with different domains.

In this chapter, an all-optically switchable dye-doped FLC grating in an alternating binary configuration with different optical properties from domain to domain is demonstrated. Figure 4.1(a) shows a conceptual diagram of the

grating which consists of static (optically isotropic) regions and tunable (optically anisotropic) regions. The side walls of each static region play a critical role on the uniform alignment of the FLC molecules in the tunable region. In this case, the polymer network structure, being constructed through the selective photo-polymerization of RMs, is utilized for producing the static region. Note that the infiltration of the FLC molecules into such polymer networks facilitates the uniform alignment of the FLC in the tunable region. Under the incident beam, the azo-compound in the dye is known to change its conformation from a rod-like *trans*-form to a bent *cis*-form [13,38-41], leading to the change of the dye-doped FLC alignment and the resultant diffraction properties. Compared to the dye-doped NLC case, the FLC grating device is capable of all-optical switching in the visible range and shows the relatively large optical modulation together with the fast response in subsecond.

## 4.2. Photoresponse of Dye-Doped Ferroelectric Liquid Crystal

Methyl red (MR), showing the reversible *trans-cis* isomerization in the visible range with the maximum absorption at the wavelength (λ) of about 500 nm, was used in this study. The MR molecules in rod-like shape (*trans*-form) favor to be mixed with the LC molecules in rod-like shape along the LC director as shown in Fig. 4.1(b) for the NLC and Fig. 4.1(c) for the FLC.

Under the pump beam at $\lambda \sim 500$ nm (544 nm in this study), the MR molecule is transformed into a bent *cis*-form and thus disturbs the alignment of the surrounding LC molecules as shown in Figs. 4.1(b)-4.1(c). Note that in the MR-doped NLC case, the optical modulation at temperatures below $T_c$ is negligibly small since the disturbance of the local orientational order by the conformation change of the MR is not sufficient to produce the LC distortions on a macroscopic level. On the other hand, in the MR-doped FLC case, the layered in-plane order of the FLC is easily disturbed by a bent *cis*-form of the MR and accordingly, the optical modulation is relatively large as depicted in Fig. 4.1(c).

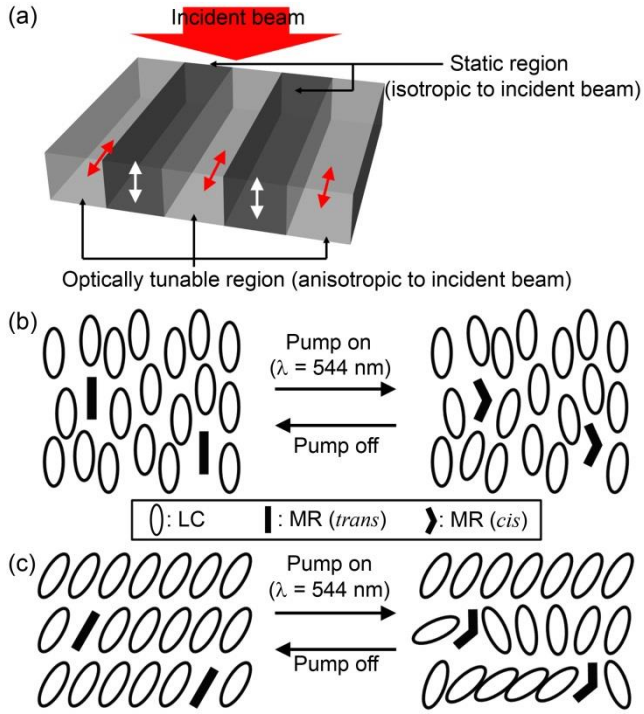


**Figure 4.1.** (a) Conceptual diagram of an optically tunable binary grating device containing the static and tunable regions. The white and red arrows denote the optic axes in the static and tunable regions, respectively. Schematic representation of the photoresponse of (b) the MR-doped NLC and (c) the MR-doped FLC. (Ref. [4])

The difference in the magnitude of the optical modulation between a dye-doped NLC and a dye-doped FLC in the cell configuration shown in Fig. 4.2(a) is first examined. Four different LC cells with the MR (Riedel-de Haen) were fabricated using ITO coated glass substrates. The homogeneous alignment layer (SE-6514H; Nissan Chemical Industries) was prepared on the inner surface of the substrate by spin coating at the rate of 3000 rpm for 30 s and rubbed unidirectionally along the direction of *R*. The cell gap was

maintained to be 5 μm using glass spacers. The rubbing directions on the top and bottom substrates were parallel to each other. The doping concentration of the MR was 2 wt%. The MR-doped LC was injected into the empty cell by capillary action. The NLCs used in this experiment were E7 ($\Delta n$ = 0.22; Merck), 5CB ($\Delta n$ = 0.18; Aldrich), and ZLI-5600-100 ($\Delta n$ = 0.17; Merck). The FLC used in this experiment was ZLI-5014-100 ($\Delta n$ = 0.12; Merck) whose helical pitch in the SmC* phase at room temperature is relatively long (> 11 μm) [64] and the cell gap of 5 μm thick was chosen to suppress the helical pitch in the surface-stabilized geometry. For each doped-LC cell, the magnitude of the optical modulation in the pump-off state and that in the pump-on state were measured using a pump-probe experiment with a photo-elastic modulator (PEM) (PEM90; Hinds Instruments) as shown in Fig. 4.2(b). The PEM with a fused silica head was placed between two crossed polarizers that were oriented at ± 45° with respect to the optic axis of the PEM head. The probe beam from a He-Ne red laser (λ = 633 nm) were set to pass the polarizer, the PEM, the sample, and the analyzer in sequence. The signal fed into a lock-in amplifier (SR830; Stanford Research System) from a photodetector was monitored as a function of the rotation angle of the sample, and the phase retardation was extracted from the first and second harmonic terms of it [65]. The intensity of the pump beam from a He-Ne green laser (λ = 544 nm) was 64 mW/cm$^2$. The polarization of the pump beam was parallel to the optic axis of the PEM head and made an angle of 45° with respect to that of the probe beam.

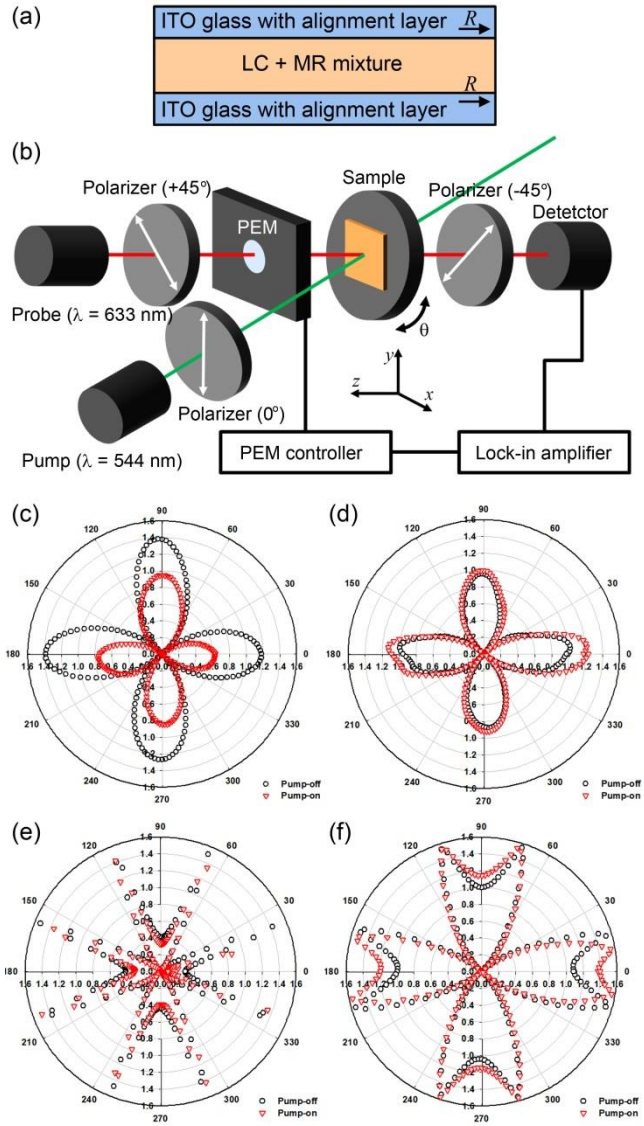


**Figure 4.2.** (a) Schematic diagram of the MR-doped LC cell. The rubbing direction is denoted by *R*. (b) Pump-probe experiment for the measurement of the optically induced phase retardation. The measured values of the optical phase retardation as a function of the azimuthal angle (θ) in the pump-off state (black circles) and the pump-

on state (red inverted triangles) for (c) the MR-doped ZLI-5014-100, (d) the MR-doped E7, (e) the MR-doped 5CB, and (f) the MR-doped ZLI-5600-100. (Ref. [4])

Figures 4.2(c)-4.2(f) show the optical retardation values for the MR-doped FLC and the three MR-doped NLCs in the pump-off and pump-on states as a function of the rotation angle of $\theta$, respectively. The circles (in black) denote the optical retardation values in the pump-off state and the inverted triangles (in red) represent those in the pump-on state. For the MR-doped FLC (ZLI-5014-100), although striped micro-domains resulting from the molecular tilt (about $\pm 10°$) in the layer were appeared, the average optic axis was nearly parallel to the rubbing direction since the micro-domains were negligibly small compared to the size of the laser spot (3 $mm^2$) used for optical retardation measurement. In this experimental geometry, the maximum value of the phase retardation ($\Gamma$) is achieved at the rotation angle of $\theta = 0°$, 90°, 180°, and/or 270° for an ideal case. Moreover, the data of the phase retardation larger than $\pi/2 = 1.57$ are represented as a pattern which is flipped over at the circumference toward the origin in the plane of the rotation angle. Figures 4.2(e) and 4.2(f) are exactly the cases. Note that the actual values of the phase retardation form four lobes whose maxima lie along the horizontal and vertical directions. It is clearly seen from Fig. 4.2(c) that among the four samples, the MR-doped FLC shows the maximum difference ($\Delta\Gamma_{max}$) in the optical retardation between the pump-off state and the pump-on state, indicating that the dye-doped FLC is indeed capable of all-optical switching. The measured values of $\Delta\Gamma_{max}$ for the MR-doped ZLI-5014-100, E7, 5CB, and

ZLI-5600-100 were 0.526, 0.104, 0.108, and 0.181, respectively. The magnitude of $\Delta\Gamma_{max}$ for the MR-doped FLC in Fig. 4.2(c) is four to five times larger than that for any of the three MR-doped NLCs shown in Figs. 4.2(d)-4.2(f) although the birefringence itself is small. This is consistent with the assertion that was expected from Figs. 4.1(b)-4.1(c).

## 4.3. Fabrication Process of Diffraction Grating

The fabrication of the MR-doped FLC grating with alternating binary domains, in one of which the FLC molecules are infiltrated into polymer networks is now described. Due to the difficulty of the uniform alignment of the FLC in the conventional grating structures such as alignment on periodic grooved polymer structures or alignment in several directions [62,63], photo-polymerized networks of the RMs were constructed in one of the binary domains to facilitate the FLC alignment in this case. In fact, the infiltration of the FLC molecules into the polymer networks enables to relieve the FLC from the elastic strain developed under the confinement between the walls of the static region. Basically, the MR-doped FLC grating was fabricated in three steps as shown in Figs 4.3(a)-(c): The first step was the exposure of the UV light onto a sample cell, where a mixture of the NLC and the RM was homogeneously aligned, through a photomask in the presence of an applied voltage to selectively form the photo-polymerized networks of the RMs in the static region as shown in Fig. 4.3(a). Note that the voltage (40 V in this case)

above the threshold should be applied to obtain an optically isotropic state, i.e., a vertically aligned state of the RMs for the static region. The preparation of the homogeneous cell and the cell gap were the same as described above. The NLC mixture was composed of the NLC (ZLI-5600-100), the RM (RM257; Merck), and the photoinitiator (4-(dimethylamino)-benzophenone; Aldrich) in the relative concentrations of 84.5 wt%, 15 wt%, and 0.5 wt%, respectively. The UV exposure was carried out for 1 s at the intensity of 70 mW/cm$^2$. The width ($w_1$) of the line pattern and the pattern period in the photomask were 100 μm and 200 μm, respectively. The second step was the removal process of the remaining NLC mixture to leave out only polymer networks in the sample cell as shown in Fig. 4.3(b). The NLC mixture was fully washed out in acetone for about 1 day. The SEM image of the part of the polymer networks formed in the static region was shown in the inset of Fig. 4.3(b). The last step was to fill the sample cell with the mixture of the FLC (ZLI-5014-100) with the MR in the relative concentrations of 98 wt% and 2 wt%, respectively, as shown in Fig. 4.3(c). The FLC mixture was injected into the sample cell in the isotropic state at 90 ℃ and slowly cooled down to room temperature at the rate of 1 ℃/min. The dimensions of the dye-doped FLC grating cell were $w_1$ = $w_2$ = 100 μm and $d$ = 5 μm, producing the stable alignment of the SmC* at room temperature in the SSFLC geometry.

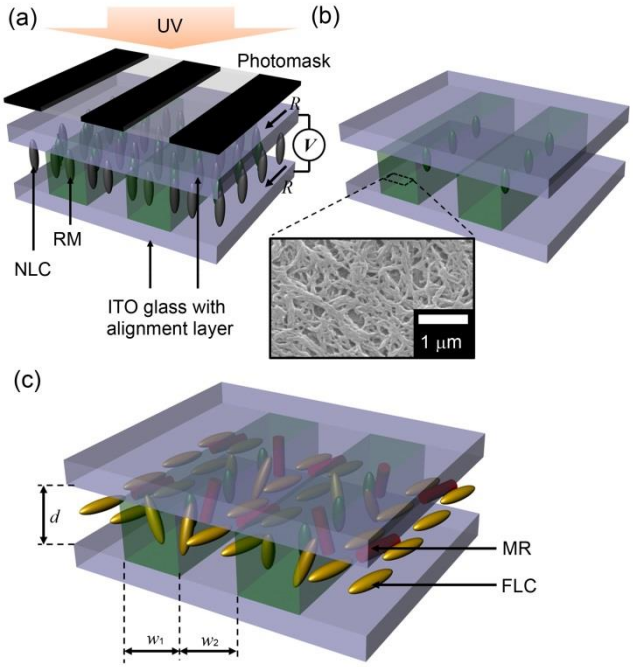


**Figure 4.3.** Schematic diagrams showing (a) the fabrication process of the binary grating structure, (b) the binary grating structure with periodic domains of vertically aligned RMs forming polymer networks (the SEM image), and (c) the MR-doped FLC grating cell. (Ref. [4])

Figure 4.4 shows the microscopic textures of the FLC grating observed with a polarizing optical microscope (Optiphot2-Pol) under crossed polarizers. The angles between the rubbing direction and the polarizer in Figs. 4.4(a)-4.4(c) were 90°, 45°, and 0°, respectively. The FLC molecules in the tunable region (region 1) were uniformly aligned along the rubbing direction while the infiltrated FLC molecules into the polymer networks in the static region (region 2) were substantially disordered as shown in Figs. 4.4(a)-4.4(c). The transmission through the static region remains nearly unchanged irrespective

of the angle between the rubbing direction and the polarizer (or the analyzer). The non-vanishing leakage of light in the static region comes from the disordered structure of the FLC molecules together with the polymer networks. It is worthwhile to note that hybrid network structures in a variety of polymer-dispersed LCs, including the blue phase [66,67], or the chiral nematic phase [68,69], have been widely used for fabricating holographic diffraction gratings, photonic nanostructures, and Bragg reflectors. In this case, the photo-polymerized networks of the RMs in the static region act as an infiltrating medium for the FLC molecules and provide an inactive domain in the optically switchable binary grating. The period of the polymer structure can be varied in the range of tens of micrometers depending on the pattern size in the used photomask.

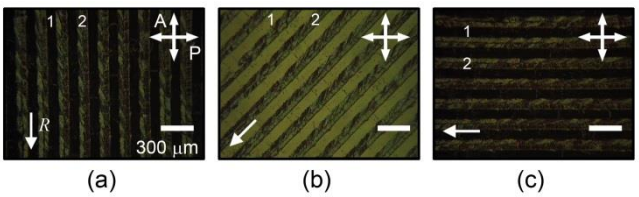


**Figure 4.4.** Microscopic textures of the MR-doped FLC grating cell under crossed polarizers when the polarizer makes angles of (a) 90°, (b) 45°, and (c) 0° with respect to the rubbing direction *R*. Region 1 is an optically tunable region and region 2 is a static region. The analyzer and the polarizer are denoted by A and P, respectively. (Ref. [4])

## 4.4. Results and Discussion

Let the diffraction properties and the optically switching capability of the MR-doped FLC grating in the pump-probe experimental geometry shown in Fig. 4.5(a) be determined. The measurements of the dynamic diffraction efficiencies of 0th and +1st order were carried out using the pump beam from a He-Ne laser with the intensity of 64 mW/cm$^2$. The polarization direction of the probe beam was set to coincide with that of the pump beam. For the incident light along the direction parallel to the surface normal of the sample, the diffraction efficiencies of 0th order ($D_0$) and ±1st order ($D_{\pm 1}$) in the binary phase grating composed of alternating anisotropic tunable regions and isotropic static (or inactive) regions can be derived from the Fraunhofer diffraction equation [1,2].

$$D_0 = \frac{1}{2}\left(\left(1+\cos\left(\frac{2\pi(n_s - n_o)d}{\lambda}\right)\right)\cos^2\phi + \left(1+\cos\left(\frac{2\pi(n_e - n_s)d}{\lambda}\right)\right)\sin^2\phi\right), \quad (4.1)$$

$$D_{\pm 1} = \frac{1}{\pi^2}\left(\left(2-2\cos\left(\frac{2\pi(n_s - n_o)d}{\lambda}\right)\right)\cos^2\phi + \left(2-2\cos\left(\frac{2\pi(n_e - n_s)d}{\lambda}\right)\right)\sin^2\phi\right), \quad (4.2)$$

where $n_e$, $n_o$, $n_s$, $\lambda$, $d$, and $\phi$ denote the extraordinary refractive index in the tunable region, the ordinary refractive index in the tunable region, the refractive index in the static region, the wavelength of the incident light, the cell gap, and the angle between the *x*-axis and the polarization direction of the incident light in Fig. 4.5(a), respectively. The two equations above show

explicitly how the diffraction efficiency depends on the difference between the refractive indices.

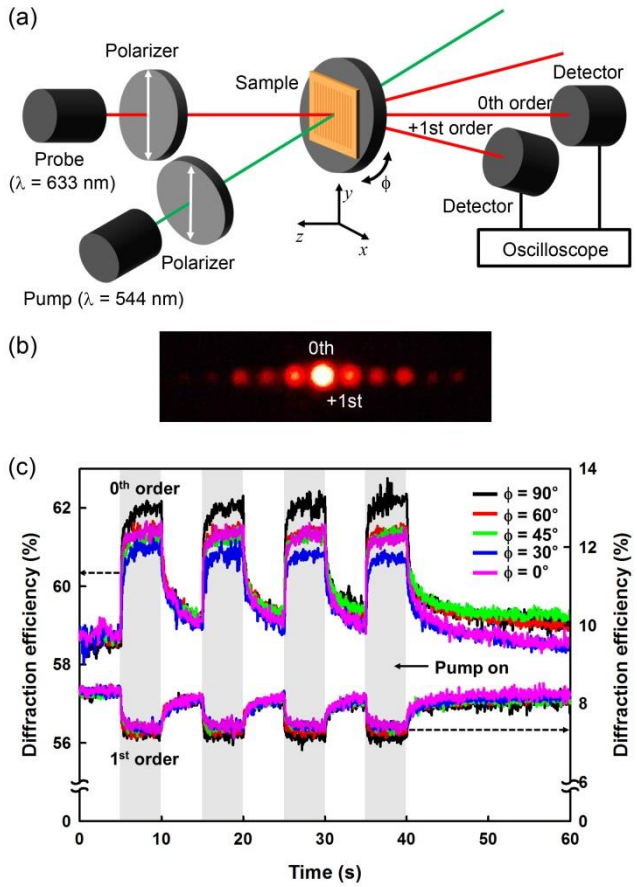


**Figure 4.5.** (a) Experimental geometry for the measurement of the dynamic diffraction properties of the MR-doped FLC grating cell. (b) The diffraction patterns observed at the rotation angle $\phi = 90°$ in the pump-off state. (c) Dynamic diffraction efficiencies of 0th and +1st orders for different values of the rotation angle $\phi$. (Ref. [4])

The diffraction patterns from the dye-doped FLC binary grating for $\phi$ = 90°, at which the maximum diffraction efficiency was achieved, were captured at the distance of about 3 m from the grating device as shown in Fig. 4.5(b). The measured diffraction efficiencies of 0th and 1st orders were about 59% and 8%, respectively. Note that the diffraction efficiency in this experiment was defined by the ratio of the diffracted intensity to the input intensity of the probe beam. Figure 4.5(c) shows all-optical switching behaviors (or the dynamic responses) of 0th and 1st orders between the pump-on and pump-off states in the FLC grating for five different values of $\phi$ = 90°, 60°, 45°, 30°, and 0°. Due to the photo-induced isomerization of the MR, the values of ($n_s$ - $n_o$) and ($n_e$ - $n_s$) were decreased in the pump-on state. Upon turning on the pump beam, for $\phi$ = 90°, the diffraction efficiency of 0th order was increased to about 62% from 59% whereas that of 1st order was slightly decreased to about 7% from 8%. In this case, the diffraction efficiency itself is quite high but the efficiency change resulting from the *trans-cis* isomerization of the MR by the pump beam is rather small due to the small changes in ($n_s$ - $n_o$) and ($n_e$ - $n_s$). The rising and falling times, $\tau_{on}$ and $\tau_{off}$, were estimated from the change of the diffraction efficiency during optical switching and they were 296 ms and 744 ms, respectively. These values are faster than most of the typical NLC gratings in optical operation. This is attributed to the fact that under the pump beam, the FLC molecules undergo the in-plane reorientation without considerable interferences among them in the layered structure whereas the NLC molecules experience severe hindrances among them in the bulk because of no positional order. In addition

to the intrinsic material properties of the FLC, the cell parameters such as the cell thickness, the pattern shape and size, and the network structure should be optimized for achieving high diffraction efficiency as well as fast optical switching of a dye-doped FLC grating

## 4.5. Summary

A new type of an all-optically switchable grating based on an azo-dye-doped FLC was constructed with the help of photo-polymerized networks of the RM molecules. The azo-doped FLC was uniformly aligned in the alternating tunable region whereas it was infiltrated into the polymer networks in the static (or optically inactive) region. The diffraction efficiency for the $0^{th}$ order in the FLC grating was found to reach at as large as 62% in the visible range and the optical response was on the order of a few hundreds of milliseconds. Although the change in the diffraction efficiency by the pump beam was rather small (from 59% to 62%) for given FLC material studied, the concept of an optically switchable FLC-based grating with high speed and high efficiency was clearly proved in the prototype device presented here. The design of a more sophisticated architecture together with the optimization of the FLC material properties and the device parameters will lead to a new class of all-optically switching components in the visible range.

# Chapter 5. Polarization-Dependent Liquid Crystal Lens Arrays

## 5.1. Introduction

Lens arrays are widely used for a variety of optical applications such as 3D displays [70-74], optical data storage devices [72-75], optical communication systems [74,76,77], and optical tweezers [73,77]. Among several types of lens arrays, LC-based lens arrays have been extensively studied due to the compactness, the easy fabrication, the high optical anisotropy, and the electrical tunability of the focal length at low voltages [73,78-83]. Since most of LC-based lens arrays were fabricated using patterned structures [74,78,79,84-86], patterned electrodes [82,84], polymer networks of the LCs [71,73,87] or surface relief structures [88], they suffered from the intrinsic drawbacks such as the limited aperture ratio and the low optical efficiency [71,78,79,82,89]. Basically, the LC is optically anisotropic and depends, in principle, on the polarization state of light. Such polarization dependence enables to design diverse optical devices including lens arrays for specific applications [74,86] but it often needs to be eliminated [90,91]. Regarding the focal length tenability of the LC-based lens arrays, both the convex lens effect and the concave lens effect were achieved depending on the difference between the ordinary and the extraordinary refractive indices of the LC [86]. Combined with the polarization dependence, the electrical tuning capability of

the focal length of the LC lens array provides more sophisticated applications such as projection-type display systems and polarization dependent imaging systems [92,93]. However, no LC-based lens array having both the polarization-dependent focal length and the fully activated areas with high optical performance has been realized so far.

## 5.2. Square Liquid Crystal Lens Array

In **Section 5.2**, a tunable LC-based square lens array with two focusing modes, one of which has a fixed focal length and the other a tunable focal length, over fully activated areas according to the polarization state of the input light is demonstrated. The refractive index of the static square lens, fabricated using a photo-curable polymer through an imprinting process, is matched with the extraordinary refractive index of the LC layer placed on the static lens. For the input beam polarized parallel to the easy axis of the LC in the homogeneous geometry, the focal length is varied with the applied voltage from a few meters to a static focal length (about 21 mm) while for the perpendicularly polarized input beam, the focal length is independent of the applied voltage and remains constant as in the static case. Note that the square lens array consists of the fully activated square areas with high uniformity and yields the polarization-dependent focal length which is electrically tunable at low voltages.

### 5.2.1. Fabrication Process

Figure 5.1(a) shows the schematic diagram of the LC-based square lens array. The bottom substrate was made of an ITO coated glass on which transparent static lenses in square shape were fabricated using the UV-curable polymer by imprinting. The top substrate consists of the ITO coated glass and the LC alignment layer which was rubbed along the direction of the *y*-axis. As an optically anisotropic medium, an LC material was placed between the two substrates. Figure 5.1(b) and 5.1(c) show the operation principles when the polarization direction of the input light coincides with the easy axis of the LC (or the rubbing direction) and is perpendicular to it, respectively. It is clear that the incident light in Fig. 5.1(b) will not be refracted due to the index-match of the LC and the polymer material while the light in Fig. 5.1(c) will experience the refraction at the LC-polymer interface by the index difference. This results in the polarization-dependent focal length tuning capability by the applied voltage.

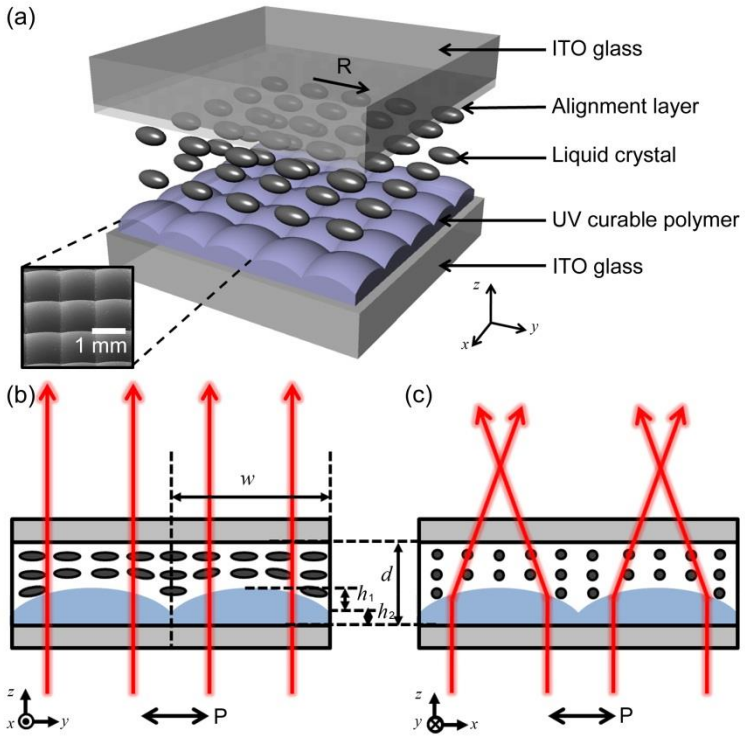


**Figure 5.1.** (a) Schematic diagram of the LC-based square lens array (R denotes the rubbing direction of the top substrate). Operation principles when the polarization direction of the input light (b) coincides with the rubbing direction and (c) is perpendicular to the rubbing direction. Here, $w$, $d$, $h_1$, $h_2$ denote the length of the side of a square lens, the cell gap, the height of the lens part, and the height of the polymer background, respectively. The inset in (a) show the SEM image of a portion the polymer lens array. (Ref. [5])

A photo-curable polymer (NOA86, $n$ = 1.55; Norland) was first prepared on an ITO coated glass by spin-coating at the rate of 1000 rpm for 20 s. The substrate was then imprinted with a master mold of the concave square lens array fabricated using PDMS. For the master mold fabrication, the PDMS was

poured on a template of a 1 mm-convex lens array (FresnelTech), subsequently cured at 90 ℃ for 12 hours, and finally detached from the template. The imprinted substrate together with the master mold was exposed to UV light at the intensity of 100 mW/cm$^2$ for 1 min. The master mold was finally peeled-off. The length ($w$) of each side and the radius of curvature ($R_c$) of a single square lens were 1 and 1.62 mm, respectively. The inset in Fig. 5.1(a) is the SEM image showing a portion of the square lens array made of the UV-curable polymer. The values of $h_1$ and $h_2$ were measured as 79.1 μm and 10 μm using a surface profiler (Alpha-step 200; KLA-TENCOR), respectively.

The homogeneous alignment layer of PI (RN-1199A; Nissan Chemical Industries, Ltd.) was prepared on the inner side of the top substrate in Fig. 5.1(a) by spin-coating at the rate of 3000 rpm for 30 s. The top substrate with the alignment layer was baked at 180 ℃ for 90 min and was unidirectionally rubbed. The bottom substrate and the top substrate were assembled such that the direction of the side of the square lens coincides with the rubbing direction. The thickness ($d$) of the LC cell was maintained using plastic spacers of 150 μm thick. A NLC (ZLI-1800-100, $n_e$ = 1.5503, $\Delta n$ = 0.0705; Merck) was finally injected into the LC cell by capillary action at room temperature. Note that since the UV-cured polymer produces the homogeneous alignment [74,3], the direction of the LC alignment on it (the bottom surface) is dictated by the rubbing direction on the other surface (the top surface) although it was not rubbed. The polarization state of the incident light on the LC-based square lens array was chosen to be either parallel or perpendicular to the rubbing axis.

## 5.2.2. Results and Discussion

Since this plano-convex type of the square lens consisting of a polymer and the LC, the focal length can be defined as $f = R_c/(n_p - n_{LC})$ in a simplified form. Here, $f$, $n_p$, $n_{LC}$, and $R_c$ denote the focal length, the refractive index of the polymer, the refractive index of the LC, and the radius of curvature of the lens, respectively. In this case, $R_c$ is 1.62 mm and $n_p$ is about 1.55 which is matched with the refractive index of the LC, at the wavelength of 589 nm [94] in the range of the visible light. Note that the wavelength dispersion is rather small for low birefringence in the range of visible light [95]. When the polarization direction of the incident light is parallel to the easy axis of the LC, $n_{LC}$ is simply $n_e$, and the focal length is then about 5400 mm. This means that the index-matched convex structure exhibits practically no lens effect at all this case. On the other hand, when the polarization direction of the incident light is perpendicular to the easy axis of the LC, $n_{LC}$ becomes $n_o$, giving the focal length of about 23.1 mm. Such polarization dependence is confirmed from Fig. 5.2 where far-field images depending on the input polarization were shown. Figure 5.2(a) depicts the experimental geometry for capturing the far-field images at the distance of 200 mm (about 9 times longer than the static focal length of 23.1 mm) away from the lens array. Figures 5.2(b) and 5.2(c) show the far-field images observed when the polarization direction (P) of the illuminated light is parallel and perpendicular to the rubbing direction (R), respectively. As expected, no focusing effect was occurred in the case that

the input polarization coincides with the rubbing direction as shown in Fig. 5.2(b).

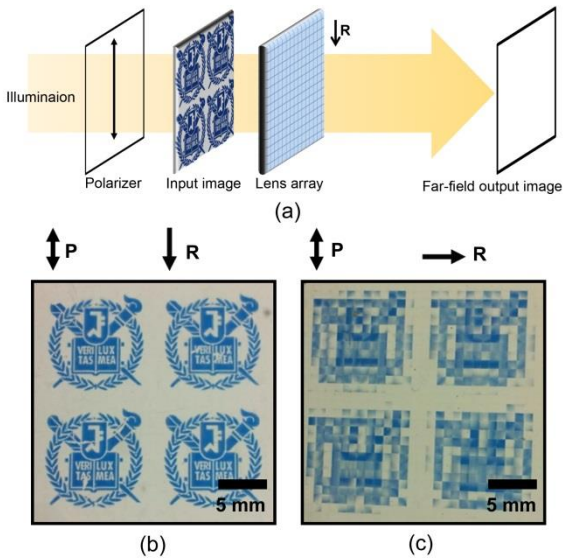


**Figure 5.2.** (a) Experimental geometry for observing far-field output images through the lens array. Photographic images of the LC-based square lens array with backlight polarized (b) parallel to the rubbing direction and (c) perpendicular to the rubbing direction. Here, P and R denote the optic axis of the polarizer and the rubbing direction on the top substrate, respectively. (Ref. [5])

Let the focusing effect of the square lens array as a function of the applied voltage be examined first with the help of a collimated laser beam at the wavelength of 543.5 nm in the focal plane as shown in Fig. 5.3(a). Figure 5.3(b) shows the charge-coupled device (CCD) images captured under the applied voltages of 0, 4, 8, and 16 V when the polarization direction of the collimated beam is parallel to the rubbing direction in the LC-based square

lens array. Clearly, the CCD images show the focusing effect. The intensity profiles of the images are shown in Fig. 5.3(b). At a relatively low voltage, the difference in the refractive index between the LC and the polymer is very small (about 0.0003) and no focusing effect appears. At a relatively high voltage of about 10 V (or the electric field of about 0.067 V/μm varying in the convex shape of the bottom substrate), the LC molecules become reoriented along the direction of the electric field (normal to the substrate) and the refractive index difference reaches at about 0.0702 which is sufficiently large to produce the focusing effect.

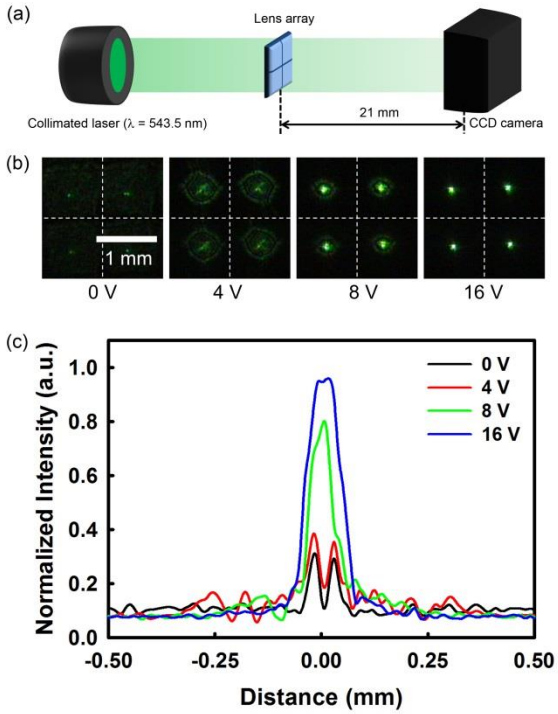


**Figure 5.3.** (a) Experimental geometry for capturing a CCD image of a collimated laser beam in the focal plane of the lens array (2 × 2). (b) The image in the focal plane under the applied voltages of 0, 4, 8, and 16 V when the polarization direction of the input light was parallel to the rubbing direction. (c) The normalized intensity profiles under several different applied voltage when the polarization direction of the input light was parallel to the rubbing direction. (Ref. [5])

The other case is shown in Fig. 5.4 where the polarization direction of the incident beam is perpendicular to the rubbing direction of the LC. It is clear from Figs. 5.4(a) and 5.4(b) that no focusing effect was essentially observed irrespective of the applied voltage, meaning that the focal length

remains unchanged. In this case, the refractive index difference is simply 0.0702 regardless of the applied voltage.

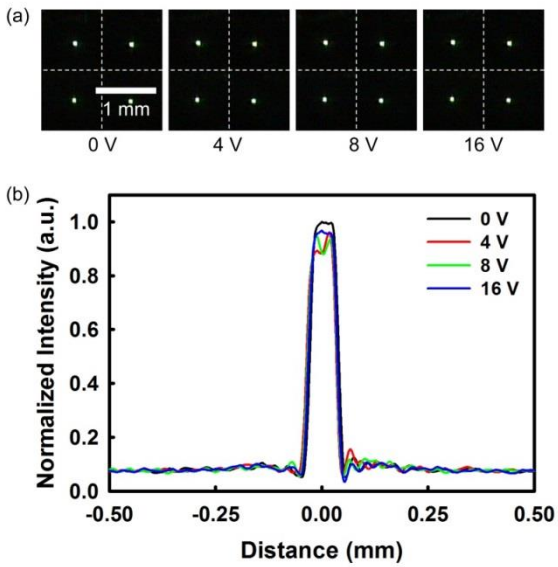


**Figure 5.4.** (a) The CCD images of a collimated laser beam in the focal plane under the applied voltages of 0, 4, 8, and 16 V when the polarization direction of the input light was perpendicular to the rubbing direction. (c) The normalized intensity profiles under several different applied voltage when the polarization direction of the input light was perpendicular to the rubbing direction. (Ref. [5])

Figure 5.5 shows the focal length variations of this LC-based square lens array measured for the two cases as a function of the applied voltage. The focal length was varied from a few meters (about 120 mm at 2 V) to 21 mm in the high voltage limit. The focal length decreases with increasing the applied voltage due to the increase of the refractive index difference between the LC

and the polymer when the polarization direction of the incident beam is parallel to the easy axis of LC. The measured focal length in the high voltage regime (about 21 mm) agrees well with the calculated value of 23.1 mm. The observed small difference may be attributed to the partial refraction occurred at the LC-polymer interface, the glass substrate-air interface, and some distortions of the LC director involved in the vicinity of the edge of the square lens. Under the applied voltage of 10 V, the rise time and fall time were measured as about 1.2 s and 30 s, respectively. The response times are quite slow due to the thick cell gap inherent to the convex shape and the dimension of the lens in the bottom substrate. The LC lens configuration, the geometrical parameters such as the intrinsic curvature of each lens and the cell gap, and the materials remain to be optimized for relatively fast switching purposes.

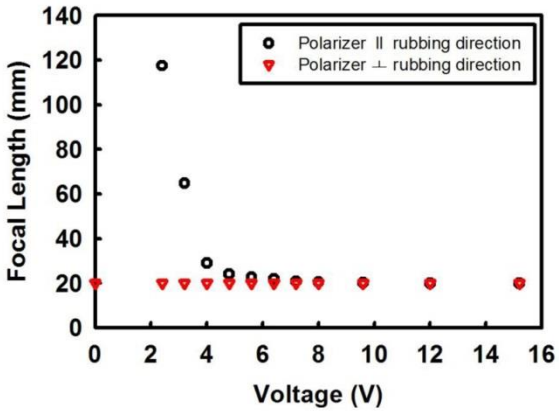


**Figure 5.5.** The focal length of the square lens array as a function of the applied voltage. (Ref. [5])

### 5.2.3. Polarization-Dependent Image Selection

The image selection capability of the LC-based square lens array depending on both the polarization state of the incident light with respect to the optic axis of the LC and the magnitude of the applied voltage is now described. The experimental geometry for selecting certain focused images according to the polarization state and the applied voltage is shown in Fig. 5.6(a). Except for only a single square lens, all other surrounding lenses were blocked to eliminate any interference among them. The input image consists of 4 different characters of “M”, “I”, “P”, and “D” arranged in two rows and two columns and located at the distance of 6 mm in front of the single square lens. The polarization states of the two columns are mutually orthogonal to each other as shown in Fig. 5.6(a). The output image focused in the real image plane was observed by the optical microscopy (Optiphot2-Pol) at the distance of 10 mm from the square lens. Figures 5.6(b) and 5.6(c) show the output images when the rubbing direction is perpendicular to the polarization direction for the letters of “M” and “P” under the applied voltages of 0 V and 10 V, respectively. As expected, only the column having “I” and “D” was defocused and focused with varying the applied voltage. The output images when the angle ($\theta$) between the rubbing direction and the polarization direction is $\theta = 45°$ under the applied voltages of 0 V and 10 V are shown in Figs. 5.6(d) and 5.6(e), respectively. In this case, all the columns were defocused and focused by the applied voltage since two orthogonal polarization components exist. In the remaining case that the rubbing

direction is parallel to the polarization direction for the letters of “M” and “P”, the output images under the applied voltages of 0 V and 10 V are shown in Figs. 5.6(f) and 5.6(g), respectively. This is exactly opposite to what were observed in the first case. It is then concluded that the image selection over an entirely activated area can be performed using the LC-based square lens through a proper combination of the input polarization state and the applied voltage.

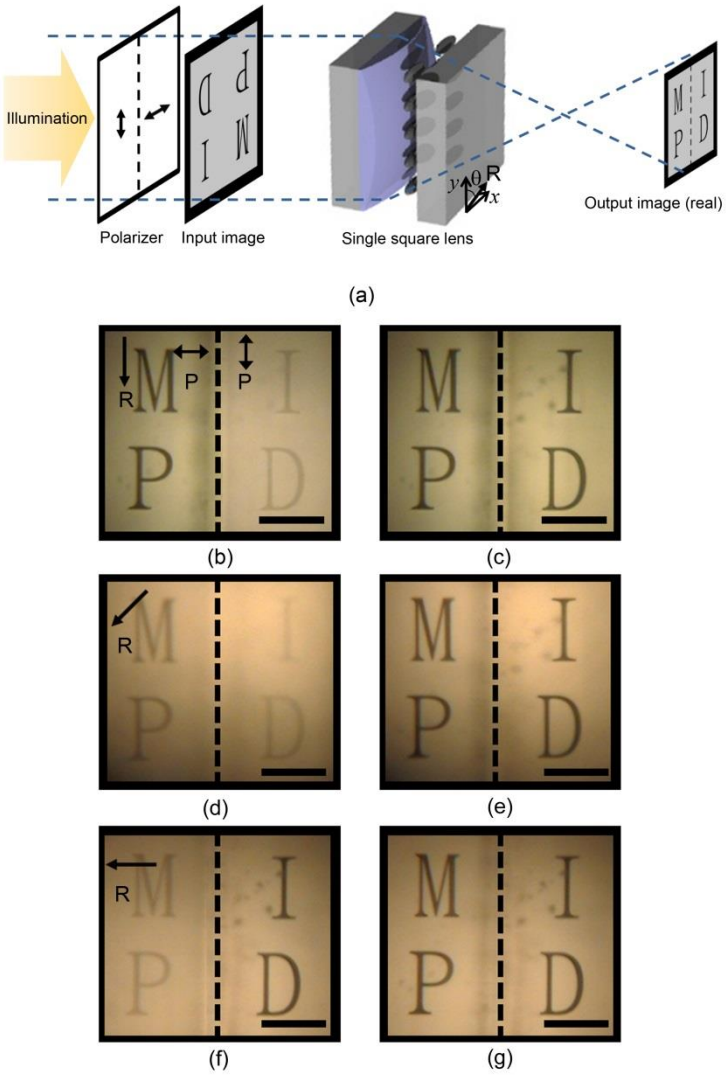


**Figure 5.6.** (a) Experimental geometry for selecting certain focused images according to the polarization state and the applied voltage. The polarization direction for the letters of “I” and “D” were mutually orthogonal to each other. The output images when the rubbing direction was perpendicular to the polarization direction for the letters of “M” and “P” under the applied voltages of (b) 0 V and (c) 10 V. The output images when the angle θ between the rubbing direction and the polarization direction

is 45° under the applied voltages of (d) 0 V and (e) 10 V. The output images when the rubbing direction was parallel to the polarization direction for the letters of “M” and “P” under the applied voltages of (f) 0 V and (g) 10 V. The scale bar is 200 μm. Here P and R denote the optic axis of the polarizers and the rubbing direction in the LC lens, respectively. (Ref. [5])

## 5.3. Lenticular Liquid Crystal Lens Array

For several decades, much effort has been made toward the realization of 3D displays in stereoscopic [96-99] and autostereoscopic types [100-108] on the basis of the binocular disparity. Recently, the stereoscopic types of 3D displays using either the shutter glasses type or the polarized glasses type have been commercialized earlier than autostereoscopic types due to their simple driving scheme and low cost. However, owing to the lack of 3D contents and the intrinsic discomfort of wearing glasses for the stereoscopic devices, the market of 3D displays has grown slower than expected. For autostereoscopic 3D displays, the use of either a parallax barrier [100-103] or a lenticular lens array [104-108] comes into the main stream of constructing the binocular disparity. The parallax barrier system has a series of slits in front of the panel, allowing each eye to see a different set of pixels. This technique is inexpensive and suitable for 2D/3D convertible displays but suffers from the low transmittance and limited viewing points [100-103]. Compared to this parallax barrier system, the lenticular lens array system requires very elaborate and expensive fabrication processes and has the difficulty of

achieving the 2D/3D switching capability although they provide superior 3D viewing properties [104-108]. Therefore, it is very important to construct a new type of a lenticular lens array, which is suitable for 2D/3D convertible displays, in a simple and cost-effective manner for the era of 3D displays.

Several types of lenticular lens arrays have been fabricated using LCs in different device configurations. One of them is a GRIN LC lens array driven by in-plane switching electrodes [109-112], periodic undulated electrodes [78,79,88], floating electrodes [73,113,114], or through the surface treatment [115,116]. A liquid crystalline polymer-based GRIN lens array combined with a twisted NLC rotator has been also suggested [117]. As shown in Fig. 5.7(a), a simple GRIN lens enables to produce the focusing effect through the modulation of the effective refractive index of LC molecules by an applied voltage. Basically, this type has inactive boundaries between two adjacent focusing regions in the LC layer due to small variations of the refractive index around the boundaries. In contrast, another type shown in Fig. 5.7(b) is more effective for the focusing capability due to the geometrical lens in addition to the index modulation of the LC [5,72,75,85,86,118]. Apart from the optical consideration, the electrode configuration should be taken into account from the viewpoint of the complexity in fabrication [73,78,79,88,109-114].

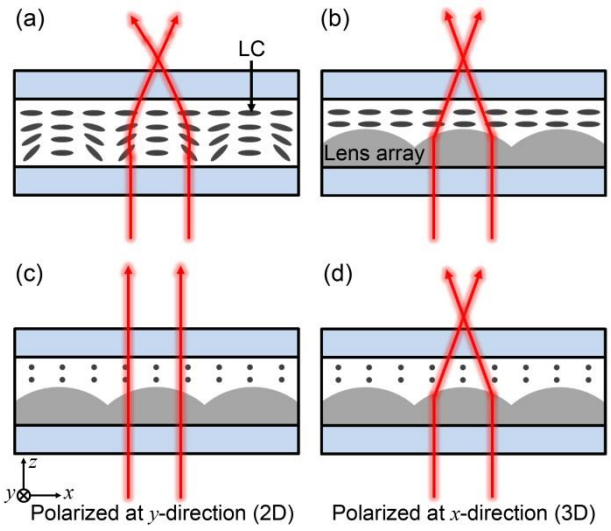


**Figure 5.7.** Schematic diagrams of (a) conventional GRIN LC lens array, (b) a static lenticular lens array with the LC layer, (c) the lenticular lens array in the 2D mode, and (d) the lenticular lens array in the 3D mode depending on the input polarization described in this section. (Ref. [6])

For the purpose of distinguishing between the 2D image and the 3D image, a new type of a lenticular lens array in which the geometrical lens and the LC layer play a complementary role in the focusing effect with respect to the input polarization as shown in Figs. 5.7(c) and 5.7(d) is proposed in **Section 5.3**. If the refractive index of the polymer used for periodic and cylindrical lenses is matched with the extraordinary refractive index of the LC medium, the incident light polarized along the *y*-direction will not be refracted and no focusing effect will be produced as shown in Fig. 5.7(c) whereas the light polarized along the *x*-direction will experience the refraction at the lens array-LC interface as depicted in Fig. 5.7(d). As a result, this lenticular lens

array is capable of distinguishing between the 2D image and the 3D image depending on the input polarization and thus, it is useful for 2D/3D convertible display systems with the excellent focusing effect provided that the input polarization is properly selected.

### 5.3.1. Fabrication Process

Figure 5.8 shows the fabrication process of the polarization-dependent lenticular lens array. A commercially available lenticular lens array sheet (Lenstar) with each lenticular lens of 257 μm wide and 234 μm of radius of curvature was used for producing a master mold of PDMS. A mixture of the PDMS precursor and the curing agent with the weight ratio of 10:1 was poured on the commercial lens sheet and treated at 100 ℃ for 1 day. The cured PDMS was then detached from the commercial lens sheet and used as master mold. Note that the lens shape, which is concave, in the PDMS mold is a replica of the convex lens shape in the commercial lens sheet. As an index matched material for fabricating the lenticular lens array, an UV-curable monomer of NOA86 was prepared on the glass substrate and pressed with the PDMS mold as shown in Fig. 5.8(a), followed by the UV exposure at the intensity of 100 $mW/cm^2$ for 20 s as shown in Fig. 5.8(b). After the PDMS mold was detached from the polymerized NOA86, the bottom substrate with the polymer lens array was finally produced. A homogeneous alignment material (RN-1199A; Nissan Chemical Industries) was spin-coated on the top

glass substrate at the speed of 3000 rpm for 30 s, and cured at 180 ℃ for 90 min. The inner surfaces of the top and bottom substrates were rubbed along the direction $R$ as shown in Fig. 5.8(c). The values of $h_1$ and $h_2$ for each polymer lenticular lens in Fig. 5.8(d) were measured to be 38.4 μm and 17.0 μm using a surface profiler (Alpha-step 200), respectively. The period $w$ and the radius of curvature $R_c$ were about 257 μm and 234 μm, respectively. The cell gap was maintained using a tape spacer (3M) of 60 μm thick. A NLC (MLC-8005; Merck) was injected into the cell by capillary action. The extraordinary refractive index and the birefringence of the LC used were $n_e$ = 1.5496 and $\Delta n$ = 0.0726, respectively.

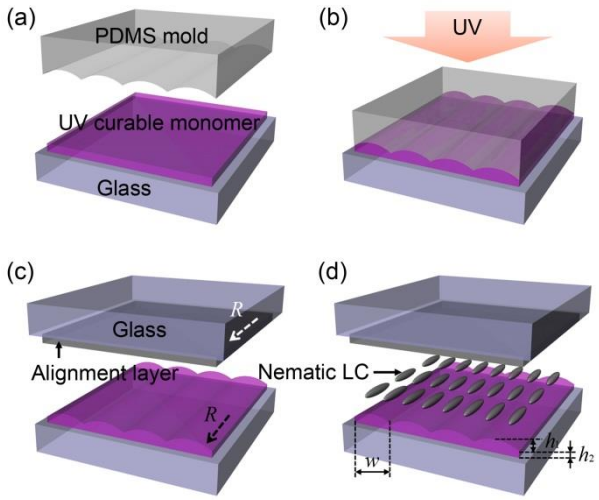


**Figure 5.8.** The fabrication processes of the lenticular lens array with the LC layer on the static polymer lens produced by simple imprinting. *R* denotes the rubbing direction. The width of each lenticular lens is *w* and the geometrical dimension is represented by $h_1$ and $h_2$. (Ref. [6])

## 5.3.2. Results and Discussion

Figures 5.9(a), 5.9(b), and 5.9(c) show the microscopic images of this LC lenticular lens array under crossed polarizers when the input polarization of the white light make angles of $\theta = 0°$, 45°, and 90° with respect to the rubbing direction, respectively. Figures 5.9(d), 5.9(e), and 5.9(f) correspond to the microscopic images observed under the green light at the wavelength $\lambda = 538$ nm. For the incoming light through the polarizer (*P*) whose polarization is either parallel or perpendicular to the rubbing direction (*R*), the outgoing light through the analyzer (*A*) experiences no phase retardation and is completely

blocked under crossed polarizers as shown in Figs. 5.9(a), 5.9(c), 5.9(d), and 5.9(f). On the other hand, as shown in Figs. 5.9(b) and 5.9(e), for the incident light whose polarization makes an angle of $\theta = 45°$ with respect to the rubbing direction, the phase retardation through the LC layer occurs and the transmission is available. Note that the LC molecules were well-aligned due to the anisotropic surface forces produced during rubbing as well as the Berreman effect [9] by periodic microstructures of polymer lens in the bottom substrate in spite of the relatively long cell gap.

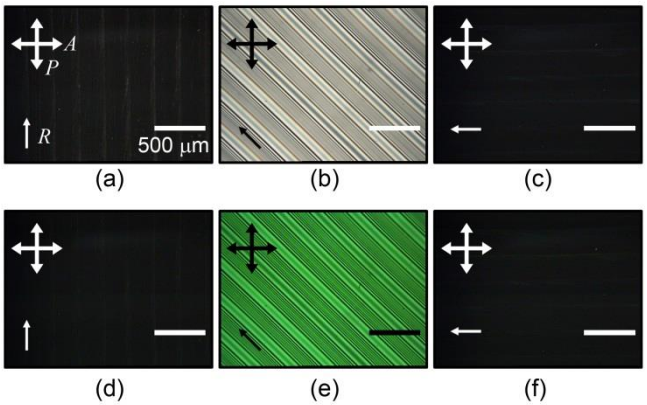


**Figure 5.9.** Microscopic images of the lenticular lens array under crossed polarizers (polarizer *P* and analyzer *A*) for different values of the angle between the input polarization and the rubbing direction. The images for the white incident light at the angle of (a) 0°, (b) 45°, and (c) 90° and those for the green incident light ($\lambda$ = 538 nm) at the angle of (d) 0°, (e) 45°, and (f) 90°. (Ref. [6])

In this lens array, the refractive index of the polymer lens ($n_p$) and the extraordinary refractive index ($n_e$) of the LC were nearly identical to each

other ($n_p$ = 1.55 and $n_e$ = 1.5496), imposing the condition of index matching for the LC molecules aligned along the lenticular lens direction. In this case of index matching, no refraction occurs at the interface between the polymer lens and the LC layer. For the incident light polarized perpendicular to the lenticular lens, however, the refraction at the interface results in the focusing effect because of no index matching between the ordinary refractive index ($n_o$) and $n_p$. The focal length ($f$) is given by $f = R_c/(n_p - n_o)$. Let the dependence of the focusing effect of this lenticular lens array on the input polarization be now described. From the values of $R_c$ = 234 μm, $n_p$ = 1.55, and $n_o$ = 1.477, for the input polarization perpendicular to the LC director, the focal length is estimated to be 3.2 mm. This agrees well with the measured focal length of 3.1 mm. The images of a collimated green beam from a He-Ne laser at λ = 543.5 nm through the fabricated lenticular lens array, captured using a CCD in the focal plane (3.1 mm away from the lenticular lens array), are shown in Figs. 5.10(a)-(e) for different values of θ ranging from 90° to 0° with respect to the rubbing direction. It is clear that the focusing effect gradually decreases with decreasing θ and eventually disappears at θ = 0°. This is exactly what is expected from this lenticular lens geometry consisting of the polymer lens and the LC layer. The degree of the focusing effect was clearly in the normalized intensity profiles presented in Fig. 5.10(b).

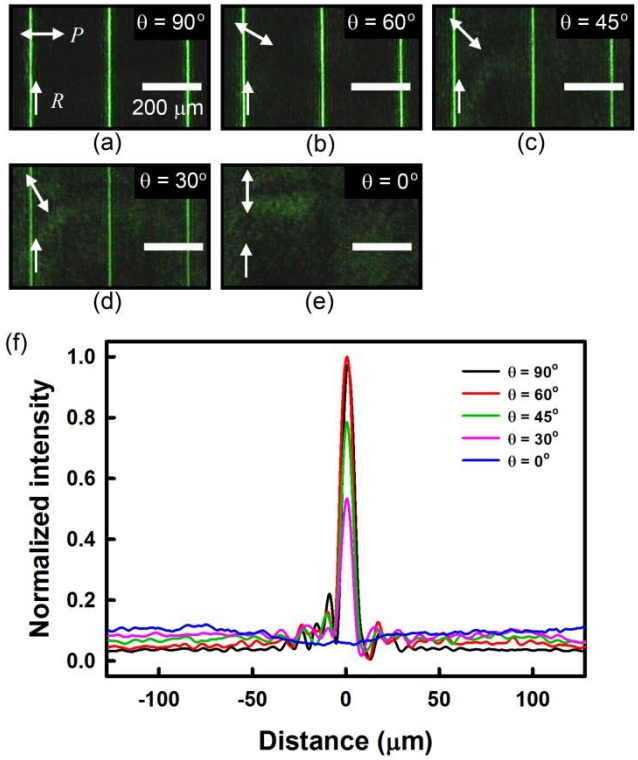


**Figure 5.10.** The CCD images of a collimated laser beam in the focal plane under crossed polarizers at the angle (a) θ = 90°, (b) θ = 60°, (c) θ = 45°, (d) θ = 30°, and (e) θ = 0° between the input polarization and the rubbing direction. (f) The normalized intensity profiles corresponding to the CCD images. (Ref. [6])

### 5.3.3. 2- and 3-Dimensional Display Applications

Now, the lenticular lens array in the 2D image mode is examined with the help of a realistic input image. From the far-field output images in Fig. 5.11(a) that were observed at the distance of 110 mm from the illuminating light source along the direction normal to the input image plane, the invariance (or

no distortion) of the image through the lenticular lens array located at the distance of 10 mm from the light source confirms that for the input polarization parallel to the rubbing direction, the lenticular lens array has indeed no focusing effect. The transmittance was about 81 %. Figures 5.11(b) and 5.11(c) show the output images observed at the viewing angles of +60° and –60°, slanted from the input image plane in the lateral direction, respectively. Clearly, the images were well preserved regardless of the viewing angle. This indicates that this lenticular lens array provides the excellent viewing properties in the 2D mode.

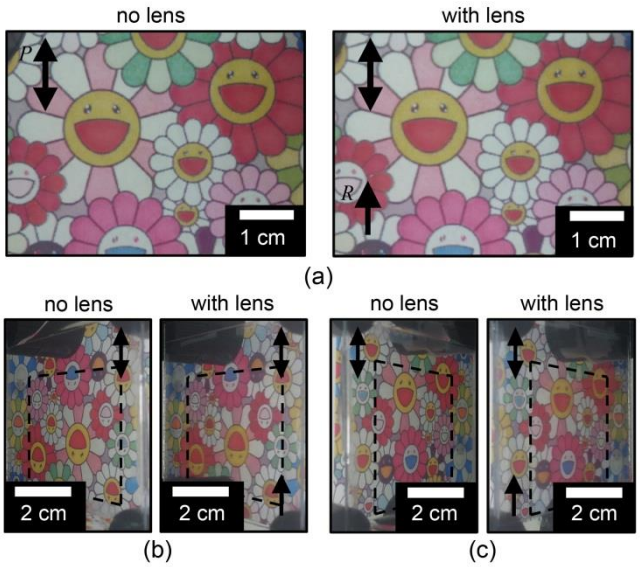


**Figure 5.11.** Far-field output images in the 2D mode without and with the lenticular lens array at the viewing angles of (a) 0°, (b) +60°, and (c) –60° with respect to the direction normal to the input image plane. (Ref. [6])

Let the focusing properties of this lenticular lens array in the 3D image mode depending on the input polarization be discussed for the realization of autostereoscopic 3D display systems [104-109]. As shown in Fig. 5.12(a), for the input polarization parallel to the rubbing direction ($\theta = 0°$), the 2D image mode was activated so that no difference between the input image and the far-field output image was observed. This is because the index matching between the polymer lens and the LC layer was achieved. The distance between the input image and the lenticular lens array was set to be 10 mm and the image was captured at the distance of 100 mm away from the lens array. On the other hand, for the input polarization perpendicular to the rubbing direction ($\theta = 90°$), the focusing effect occurs due to the refraction at the interface between the polymer lens and the LC layer. As a result, the far-field output image, being not in the focal plane at 3.1 mm from the lens array, becomes blurred as shown Fig. 5.12(b). Based on the polarization-dependent focusing effect described above, this lenticular lens array is directly applicable for constructing autostereoscopic 2D/3D convertible display systems when it is combined with an optical element for the polarization rotator between the backlight and the lens array [117]. It should be noted that electrically switchable lens arrays with embedded electrodes [5,109] are simple in operation but exhibit the slow response due to the relatively thick cell gap. Instead, this type of the lenticular lens needs an additional polarizer rotator for 2D/3D convertible displays.

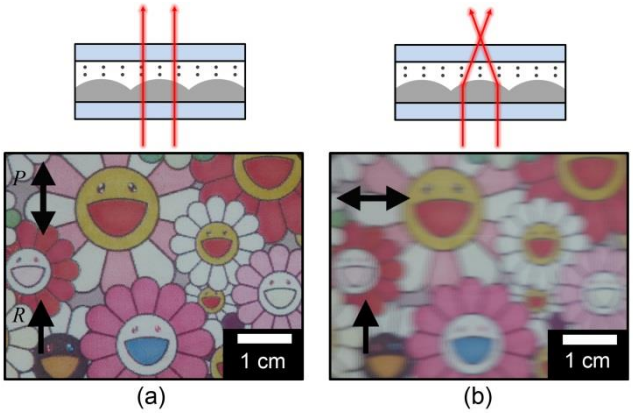


**Figure 5.12.** Far-field output images in the 2D mode and the 3D mode with the lenticular lens array for the input polarization (a) parallel and (b) perpendicular to the rubbing direction. The non-focusing and focusing properties are shown in the insets. (Ref. [6])

## 5.4. Summary

An electrically LC-based square lens array with fully activated areas that exhibit two focusing modes with fixed and tunable focal lengths according to the polarization state of the incident light was constructed. There are two essential issues on the fabrication of such LC-based square lens array; one is the index-matching between the LC and the photo-curable polymer material. The other is to tailor the tuning range of the primary focal length in terms of the radius of curvature of an individual square lens. In the case of fabricated square LC lens array, the focal length was varied from a few meters to 21 mm for the radius of curvature $R_c$ ~ 1.62 mm, the refractive index of the polymer $n_p$ ~ 1.55, and the birefringence of the LC $\Delta n$ ~ 0.071. The tunable square lens

array will be applicable for building up advanced imaging systems and displays requiring precise selection of the focused images in space by space according to the input polarization and the applied voltage. An LC-based lenticular lens array with the polarization-dependent focusing effect arising from the LC on the polymer lens was also constructed by the simple imprinting technique. The input polarization-dependence of this LC lenticular lens array arises mainly from the index matching scheme between the polymer lenticular lens and the LC on it. This lenticular lens array show excellent 2D-viewing properties irrespective of the viewing angle and allow the focusing effect for 3D imaging which depends on the radius of curvature of the static polymer lens together with the refractive indices ($n_o$ and $n_e$) of the LC used. It can be directly applicable for autostereoscopic 2D/3D convertible displays in combination with an optical element for the input polarization rotator.

# Chapter 6. Concluding Remarks

In this thesis, new concepts of LC diffraction gratings and LC lens arrays suitable for more advanced optical devices were demonstrated. Based on the basic properties of LC such as wide tuning capability of the optical properties resulting from the large change of the optical and/or electro-optical anisotropy under small external perturbations, the self-organizing nature, the fluidity with long-range order, and the design flexibility on various substrates, an electrically tunable LC grating with continuous LC alignment geometry, an optically switchable FLC binary grating, and polarization-dependent LC lens arrays were fabricated using simple and cost-effective processes.

Firstly, a new type of the LC grating device possessing the continuously graded phase retardation within an individual grating pattern was demonstrated. The fully continuous phase retardation was achieved using the semi-circular alignment of the LC on a micro-grooved substrate fabricated through an imprinting process. This continuous LC grating with rotation symmetry exhibited the switching effect between the diffraction orders of 0th and ±1st. The continuous grating architecture with high symmetry presented here will be applicable for devising a variety of optical elements including a tunable beam splitter and a switchable diffractive component.

Secondly, a new type of an all-optically switchable grating based on an azo-dye-doped FLC was constructed with the help of photo-polymerized networks of the RM molecules. The azo-doped FLC was uniformly aligned in

the alternating tunable region whereas it was infiltrated into the polymer networks in the static (or optically inactive) region. The diffraction properties this FLC grating was found to be switched in the visible range and the optical response was on the order of a few hundreds of milliseconds. Although the change in the diffraction efficiency by the pump beam was rather small for given FLC material studied, the concept of an optically switchable FLC-based grating with high speed and high efficiency was clearly proved in the prototype device presented here. The design of a more sophisticated architecture together with the optimization of the FLC material properties and the device parameters will lead to a new class of all-optically switching components in the visible range.

Thirdly, two polarization-dependent LC lens arrays were demonstrated. An electrically LC-based square lens array with fully activated areas that exhibit two focusing modes with fixed and tunable focal lengths according to the polarization state of the incident light was constructed at first. There were essential issues on the fabrication of such LC-based square lens array including the index-matching between the LC and the photo-curable polymer material and tailoring the tuning range of the primary focal length in terms of the radius of curvature of an individual square lens. The tunable square lens array will be applicable for building up advanced imaging systems and displays requiring precise selection of the focused images in space by space according to the input polarization and the applied voltage. In addition, an LC-based lenticular lens array with the polarization-dependent focusing effect arising from the LC on the polymer lens fabricated by simple imprinting was

also constructed. The input polarization-dependence of this LC lenticular lens array arises mainly from the index matching scheme between the polymer lenticular lens and the LC on it. Our lenticular lens array showed excellent 2D-viewing properties irrespective of the viewing angle and allowed the focusing effect for 3D imaging which depends on the radius of curvature of the static polymer lens together with the refractive indices ($n_o$ and $n_e$) of the LC used. It can be directly applicable for autostereoscopic 2D/3D convertible displays in combination with an optical element for the input polarization rotator.

In conclusion, throughout this thesis, new types of advanced LC diffraction gratings including electrically tunable LC grating having continuous alignment geometry and optically switchable FLC binary grating with superb switching capability were explored. Moreover, LC square lens array and LC lenticular lens array with perfect polarization-dependence were also described. These studies were carried out from the viewpoint of the expansion of the applications of these fundamental optical components to various optical systems with more sophisticated functions. These advanced fundamental optical components will be useful for devising a variety of sophisticated optical systems.

# Appendix (acronyms)

2D: two-dimensional

3D: three-dimensional

CCD: charge-coupled device

FLC: ferroelectric liquid crystal

GRIN: gradient refractive index

ITO: indium-tin-oxide

LC: liquid crystal

LCD: liquid crystal display

MR: methyl red

NLC: nematic liquid crystal

PDMS: poly(dimethylsiloxane)

PEM: photo-elastic modulator

PI: polyimide

RM: reactive mesogen

SEM: scanning electron microscopy

SmA: smectic A

SmC: smectic C

SmC*: chiral smectic C

SSFLC: surface stabilized ferroelectric liquid crystal

UV: ultraviolet

# Bibliography


[1] B. E. A. Saleh and M. C. Teich, *Fundamentals of photonics*, Wiley-Interscience Publications, Cananda (1991).

[2] J. W. Goodman, *Introduction to Fourier optics*, McGraw-Hill, USA (1968).

[3] J. Kim, J.-H. Na, and S.-D. Lee, *Opt. Express* **20**, 3034 (2012).

[4] J. Kim, J.-H. Suh, B.-Y. Lee, S.-U. Kim, and S.-D. Lee, *Opt. Express* **23**, 12619 (2015).

[5] J. Kim, J. Kim, J.-H. Na, B. Lee, and S.-D. Lee, *Opt. Express* **22**, 3316 (2014).

[6] J. Kim, S.-U. Kim, B.-Y. Lee, J.-H. Suh, and S.-D. Lee, *J. Inf. Disp.* **16**, 11 (2015).

[7] P. J. Collings, *Liquid crystals: Nature's delicate phase of matter*, Princeton University Press, UK (1990).

[8] V. G. Chigrinov, *Liquid crystal devices: Physics and applications*, Artech House, USA (1999).

[9] D. W. Berreman, *Phys. Rev. Lett.* **28**, 1683 (1972).

[10] C. W. Oseen, *Trans. Faraday Soc*. **29**, 883 (1993).

[11] F. C. Frank, *Disc. Faraday Soc.* **25**, 19 (1958).

[12] A. Rapini and M. J. Papoular, *J. Phys. (Paris) Colloq.* **30**, C4 (1969).

[13] T. Ikeda, *J. Mater. Chem.* **13**, 2037 (2003).

[14] M. Ivanov and T. Eiju, *Proc. SPIE* **4580**, 664 (2001).

[15] J. A. Davis, J. Adachi, C. R. Fernández-Pousa, and I. Moreno, *Opt. Lett.* **26**, 587 (2001).

[16] E. Hasman, Z. Bomzon, A. Niv, G. Biener, and V. Kleiner, *Opt. Commun.* **209**, 45 (2002).

[17] S. Jung, J.-H. Park, H. Choi, and B. Lee, *Appl. Opt.* **42**, 2513 (2003).

[18] S. R. Nersisyan, N. V. Tabiryan, D. M. Steeves, and B. R. Kimball, *Opt. Photonics News* **21**, 40 (2010).

[19] S. R. Nersisyan, N. V. Tabiryan, D. M. Steeves, and B. R. Kimball, *J. Nonlinear Opt. Phys. Mater.* **18**, 1 (2009).

[20] M. Le Doucen and P. Pellat-Finet, *Opt. Commun.* **151**, 321 (1998).

[21] J. Chen, P. J. Bos, H. Vithana, and D. L. Johnson, *Appl. Phys. Lett.* **67**, 2588 (1995).

[22] C. M. Titus and P. J. Bos, *Appl. Phys. Lett.* **71**, 2239 (1997).

[23] Z. He and S. Sato, *Appl. Opt.* **37**, 6755 (1998).

[24] B. Wen, R. G. Petschek, and C. Rosenblatt, *Appl. Opt.* **41**, 1246 (2002).

[25] C.-J. Yu, D.-W. Kim, J. Kim, and S.-D. Lee, *Opt. Lett.* **30**, 1995 (2005).

[26] J.-H. Park, I. C. Khoo, C.-J. Yu, M.-S. Jung, and S.-D. Lee, *Appl. Phys. Lett.* **86**, 021906 (2005).

[27] E. Jang, H.-R. Kim, Y.-J. Na, and S.-D. Lee, *Appl. Phys. Lett.* **91**, 071109 (2007).

[28] M. Zhu, G. Carbone, and C. Rosenblatt, *Appl. Phys. Lett.* **88**, 253502 (2006).

[29] C. Provenzano, P. Pagliusi, and G. Cipparrone, *Appl. Phys. Lett.* **89**, 121105 (2006).

[30] H. Sarkissian, S. V. Serak, N. V. Tabiryan, L. B. Glebov, V. Rotar, and B. Y. Zeldovich, *Opt. Lett.* **31**, 2248 (2006).

[31] C. Oh and M. J. Escuti, *Opt. Lett.* **33**, 2287 (2008).

[32] V. Presnyakov, K. Asatryan, T. Galstian, and V. Chigrinov, *Opt. Express* **14**, 10558 (2006).

[33] J.-C. Chao, W.-Y. Wu, and A. Y.-G. Fuh, *Opt. Express* **15**, 16702 (2007).

[34] M. Honma and T. Nose, *Appl. Opt.* **43**, 5193 (2004).

[35] N. Bennis, M. A. Geday, X. Quintana, B. Cerrolaza, D. P. Medialdea, A. Spadlo, R. Dabrowski, and J. M. Oton, *Opto-Electron. Rev.* **17**, 112 (2009).

[36] Y.-W. Lim, C.-H. Kwak, and S.-D. Lee, *J. Nanosci. Nanotechnol.* **8**, 4775 (2008).

[37] J. Kim, Y.-W. Lim, J.-H. Na, and S.-D. Lee, *Appl. Opt.* **52**, 1752 (2013).

[38] D. E. Lucchetta, F. Vita, and F. Simoni, *Appl. Phys. Lett.* **97**, 231112 (2010).

[39] Y. J. Liu, Y. B. Zheng, J. Shi, H. Huang, T. R. Walker, and T. J. Huang,

*Opt. Lett.* **34**, 2351 (2009).

[40] L. De Sio, J. G. Cuennet, A. E. Vasdekis, and D. Psaltis, *Appl. Phys. Lett.* **96**, 131112 (2010).

[41] L. De Sio, A. E. Vasdekis, J. G. Cuennet, A. De Luca, A. Pane, and D. Psaltis, *Opt. Express* **19**, 23532 (2011).

[42] H.-R. Kim, E. Jang, J. Kim, K.-I. Joo, and S.-D. Lee, *Appl. Opt.* **51**, 8526 (2012).

[43] L. De Sio, A. Veltri, C. Umeton, S. Serak, and N. Tabiryan, *Appl. Phys. Lett.* **93**, 181115 (2008).

[44] X. Tong, G. Wang, A. Yavrian, T. Galstian, and Y. Zhao, *Adv. Mater.* **17**, 370 (2005).

[45] L. De Sio, S. Serak, N. Tabiryan, S. Ferjani, A. Veltri, and C. Umeton, *Adv. Mater.* **22**, 2316 (2010).

[46] H. Jashnsaz, N. H. Nataj, E. Mohajerani, and A. Khabbazi, *Appl. Opt.* **50**, 4295 (2011).

[47] S.-Y. Huang, T.-C. Tung, H.-C. Jau, J.-H. Liu, and A. Y.-G. Fuh, *Appl. Opt.* **50**, 5883 (2011).

[48] G. Gilardi, L. De Sio, R. Beccherelli, R. Asquini, A. d'Alessandro, and C. Umeton, *Opt. Lett.* **36**, 4755 (2011).

[49] D. C. Zografopoulos, R. Asquini, E. E. Kriezis, A. d'Alessandro, and R. Beccherelli, *Lab Chip* **12**, 3598 (2012).

[50] M. Shian Li, A. Y.-G. Fuh, and S.-T. Wu, *Opt. Lett.* **36**, 3864 (2011).

[51] M. S. Li, A. Y.-G. Fuh, J.-H. Liu, and S.-T. Wu, *Opt. Express* **20**, 25545 (2012).

[52] V. Caligiuri, L. De Sio, L. Petti, R. Capasso, M. Rippa, M. G. Maglione, N. Tabiryan, and C. Umeton, *Adv. Opt. Mater.* **2**, 950 (2014).

[53] R. P. Lemieux, *Soft Matter* **1**, 348 (2005).

[54] H.-K. Lee, A. Kanazawa, T. Shiono, T. Ikeda, T. Fujisawa, M. Aizawa, and B. Lee, *Chem. Mater.* **10**, 1402 (1998).

[55] G. P. Crawford, J. N. Eakin, M. D. Radcliffe, A. Callan-Jones, and R. A. Pelcovits, *J. Appl. Phys.* **98**, 123102 (2005).

[56] J. G. Cuennet, A. E. Vasdekis, L. De Sio, and D. Psaltis, *Nat. Photonics* **5**, 234 (2011).

[57] H. J. Coles, H. G. Walton, D. Guillon, and G. Poetti, *Liq. Cryst.* **15**, 551 (1993).

[58] J. Guan, M. Zhang, W. Gao, H. Yang, and G. Wang, *ChemPhysChem* **13**, 1425 (2012).

[59] T. Ikeda, T. Sasaki, and K. Ichimura, *Nature* **361**, 428 (1993).

[60] Y. Lansac, M. A. Glaser, N. A. Clark, and O. D. Lavrentovich, *Nature* **398**, 54 (1999).

[61] T. Inoue and Y. Tomita, *J. Opt. Soc. Am. B* **13**, 1916 (1996).

[62] A. K. Srivastava, W. Hu, V. G. Chigrinov, A. D. Kiselev, and Y.-Q. Lu,

*Appl. Phys. Lett.* **101**, 031112 (2012).

[63] S. J. Woltman, J. N. Eakin, G. P. Crawford, and S. Zumer, *Opt. Lett.* **31**, 3273 (2006).

[64] Data sheet of ZLI-5014–100 provided by Merck, Ltd.

[65] F. Zhang and J. W. Lit, *Appl. Opt.* **32**, 2213 (1993).

[66] F. Castles, F. V. Day, S. M. Morris, D.-H. Ko, D. J. Gardiner, M. M. Qasim, S. Nosheen, P. J. W. Hands, S. S. Choi, R. H. Friend, and H. J. Coles, *Nat. Mater.* **11**, 599 (2012).

[67] J. Xiang and O. D. Lavrentovich, *Appl. Phys. Lett.* **103**, 051112 (2013).

[68] M. E. Sousa, D. J. Broer, C. W. M. Bastiaansen, L. B. Freund, and G. P. Crawford, *Adv. Mater.* **18**, 1842 (2006).

[69] S. S. Choi, S. M. Morris, W. T. S. Huck, and H. J. Coles, *Adv. Mater.* **22**, 53 (2010).

[70] L. Dong, A. K. Agarwal, D. J. Beebe, and H. Jiang, *Nature* **442**, 551 (2006).

[71] H. Ren and S.-T. Wu, *Appl. Phys. Lett.* **82**, 22 (2003).

[72] H. Ren, J. R. Wu, Y.-H. Fan, Y.-H. Lin, and S.-T. Wu, *Opt. Lett.* **30**, 376 (2005).

[73] H.-C. Lin and Y.-H. Lin, *Opt. Express* **20**, 2045 (2012).

[74] Y. Choi, H.-R. Kim, K.-H. Lee, Y.-M. Lee, and J.-H. Kim, *Appl. Phys. Lett.* **91**, 221113 (2007).

[75] H. R. Stapert, S. del Valle, E. J. K. Verstegen, B. M. I. van der Zande, J. Lub, and S. Stallinga, *Adv. Funct. Mater.* **13**, 732 (2003).

[76] Y. Lu, Y. Yin, and Y. Xia, *Adv. Mater.* **13**, 34 (2001).

[77] C. H. Sow, A. A. Bettiol, Y. Y. G. Lee, F. C. Cheong, C. T. Lim, and F. Watt, *Appl. Phys. B* **78**, 705 (2004).

[78] H. Ren, Y.-H. Fan, S. Gauza, and S.-T. Wu, *Appl. Phys. Lett.* **84**, 4789 (2004).

[79] W. Choi, D.-W. Kim, and S.-D. Lee, *Mol. Cryst. Liq. Cryst. (Phila. Pa.)* **508**, 35 (2009).

[80] Y. Li and S.-T. Wu, *Opt. Express* **19**, 8045 (2011).

[81] Y.-H. Lin, H.-S. Chen, H.-C. Lin, Y.-S. Tsou, H.-K. Hsu, and W.-Y. Li, *Appl. Phys. Lett.* **96**, 113505 (2010).

[82] C. J. Hsu and C. R. Sheu, *Opt. Express* **20**, 4738 (2012).

[83] L. Lucchetti and J. Tasseva, *Appl. Phys. Lett.* **100**, 181111 (2012).

[84] M. Hain, R. Glockner, S. Bhattacharya, D. Dias, S. Stankovic, and T. Tschudi, *Opt. Commun.* **188**, 291 (2001).

[85] H. Ren, Y.-H. Fan, and S.-T. Wu, *Opt. Lett.* **29**, 1608 (2004).

[86] H. T. Dai, Y. J. Liu, X. W. Sun, and D. Luo, *Opt. Express* **17**, 4317 (2009).

[87] V. V. Presnyakov, K. E. Asatryan, T. V. Galstian, and A. Tork, *Opt. Express* **10**, 865 (2002).

[88] J.-H. Na, S. C. Park, S.-U. Kim, Y. Choi, and S.-D. Lee, *Opt. Express* **20**, 864 (2012).

[89] K. Asatryan, V. Presnyakov, A. Tork, A. Zohrabyan, A. Bagramyan, and T. Galstian, *Opt. Express* **18**, 13981 (2010).

[90] J.-H. Lee, H.-R. Kim, and S.-D. Lee, *Appl. Phys. Lett.* **75**, 859 (1999).

[91] D.-W. Kim, C.-J. Yu, H.-R. Kim, S.-J. Kim, and S.-D. Lee, *Appl. Phys. Lett.* **88**, 203505 (2006).

[92] J. Hong, Y. Kim, S.-G. Park, J.-H. Hong, S.-W. Min, S.-D. Lee, and B. Lee, *Opt. Express* **18**, 20628 (2010).

[93] Y. Kim, K. Hong, J. Yeom, J. Hong, J.-H. Jung, Y. W. Lee, J.-H. Park, and B. Lee, *Opt. Express* **20**, 20130 (2012).

[94] Data sheet of ZLI-1800–100 provided by Merck, Ltd.

[95] S.-T. Wu, *Phys. Rev. A* **33**, 1270 (1986).

[96] L. Zhang and W. J. Tam, *IEEE Trans. Broadcast.* **51**, 191 (2005).

[97] Y.-J. Wu, Y.-S. Jeng, P.-C. Yeh, C.-J. Hu, and W.-M. Huang, *SID Symp. Digest Tech. Pap.* **39**, 260 (2008).

[98] G. D. Love, D. M. Hoffman, P. J. W. Hands, J. Gao, A. K. Kirby, and M. S. Banks, *Opt. Express* **17**, 15716 (2009).

[99] M. Barkowsky, S. Tourancheau, K. Brunnstrom, K. Wang, and B. Andren, *SID Symp. Digest Tech. Pap.* **42**, 812 (2011).

[100] C.-H. Chen, Y.-P. Huang, S.-C. Chuang, C.-L. Wu, H.-P. D. Shieh, W. Mphepo, C.-T. Hsieh, and S.-C. Hsu, *Appl. Opt.* **48**, 3446 (2009).

[101] Y. Jung, J.-M. Kim, J. Kim, H. Sung, S.-W. Min, and S.-W. Lee, *Opt. Eng.* **53**, 025101 (2014).

[102] J.-Y. Luo, Q.-H. Wang, W.-X. Zhao, and D.-H. Li, *Appl. Opt.* **50**, 2911 (2011).

[103] H. Yamamoto, M. Kouno, S. Muguruma, Y. Hayasaki, Y. Nagai, Y. Shimizu, and N. Nishida, *Appl. Opt.* **41**, 6907 (2002).

[104] G. J. Woodgate and J. Harrold, *SID Symp. Digest Tech. Pap.* **36**, 378 (2005).

[105] Y.-Y. Kao, Y.-P. Huang, K.-X. Yang, P. C.-P. Chao, C.-C. Tsai, and C.-N. Mo, *SID Symp. Digest Tech. Pap.* **40**, 111 (2009).

[106] W. L. IJzerman, S. T. de Zwart, and T. Dekker, *SID Symp. Digest Tech. Pap.* **36**, 98 (2005).

[107] Y.-G. Lee and J. B. Ra, *Opt. Eng.* **45**, 017007 (2006).

[108] K. C. Heo, S. H. Yu, J. H. Kwon, and J. S. Gwag, *Appl. Opt.* **52**, 8460 (2013).

[109] Y.-H. Lin, H. Ren, K.-H. Fan-Chiang, W.-K. Choi, S. Gauza, X. Zhu, and S.-T. Wu, *Jpn. J. Appl. Phys.* **44**, 243 (2005).

[110] H. Ren, S. Xu, Y. Liu, and S.-T. Wu, *Opt. Express* **21**, 29304 (2013).

[111] M. Kawamura, K. Nakamura, and S. Sato, *Opt. Express* **21**, 26520 (2013).

[112] Y.-C. Chang, T.-H. Jen, C.-H. Ting, and Y.-P. Huang, *Opt. Express* **22**, 2714 (2014).

[113] Y.-H. Lin and H.-S. Chen, *Opt. Express* **21**, 9428 (2013).

[114] L. Li, D. Bryant, T. V. Heugten, and P. J. Bos, *Opt. Express* **21**, 8371 (2013).

[115] L. Lu, V. Sergan, T. V. Heugten, D. Duston, A. Bhowmik, and P. J. Bos, *Opt. Express* **21**, 7133 (2013).

[116] F. Fan, A. K. Srivastava, T. Du, M. C. Tseng, V. Chigrinov, and H. S. Kwok, *Opt. Lett.* **38**, 4116 (2013).

[117] H. Ren, S. Xu, Y. Liu, and S.-T. Wu, *Opt. Express* **21**, 7916 (2013).

[118] S.-U. Kim, S. Lee, J.-H. Na, and S.-D. Lee, *Opt. Commun.* **313**, 329 (2014).

# Publications

## [1] International Journals

1. S.-H. Lee, I.-H. Lee, **J. Kim**, C.-M. Keum, E.-S. Yu, and S.-D. Lee, "Electrowetting-on-dielectric device controlled by embedded undulating electrode for liquid transport", *J. Nanosci. Nanotechnol.* (Accepted).

2. S.-U. Kim, **J. Kim**, E.-S. Yu, I.-H. Lee, B.-Y. Lee, Y. Sohn, and S.-D. Lee, "Colloidal assembling template with wrinkled patterns based on liquid crystalline polymer", *Mol. Cryst. Liq. Cryst.* (Accepted).

3. J.-H. Suh, **J. Kim**, Y.-S. Ryu, Y. Sohn, and S.-D. Lee, "Control of surface anchoring properties of liquid crystal by thermo-transfer printing of siloxane oligomers", *Liq. Cryst.* (Published online).

4. **J. Kim**, J.-H. Suh, B.-Y. Lee, S.-U. Kim, and S.-D. Lee, "Optically switchable grating based on dye-doped ferroelectric liquid crystal with high efficiency", *Opt. Express* **23**, 12619 (2015).

5. S.-U. Kim, **J. Kim**, and S.-D. Lee, "Precise lens-on-lens architecture using selective wettability for image-depth representation", *Mol. Cryst. Liq. Cryst.* **595**, 50 (2014).

6. **J. Kim**, J. Kim, J.-H. Na, B. Lee, and S.-D. Lee, "Liquid crystal-based square lens array with tunable focal length", *Opt. Express* **22**, 3316 (2014).

7. J.-H. Na, **J. Kim**, Y. Choi, and S.-D. Lee, "Topographic confinement of a ferroelectric liquid crystal for highly efficient tunable electrooptic effect with reduced threshold", *Appl. Phys. Express* **6**, 054102 (2013).

8. **J. Kim**, Y.-W. Lim, J.-H. Na, and S.-D. Lee, "Tunable binary retarder using self-aligned liquid crystal on anisotropic polymer film by photo-assisted imprinting", *Appl. Opt.* **52**, 1752 (2013).

9. H.-R. Kim, E. Jang, **J. Kim**, J.-I. Joo, and S.-D. Lee, "Dynamic polarization grating based on a dye-doped liquid crystal controllable by a single beam in a homeotropic-planar geometry", *Appl. Opt.* **51**, 8526 (2012).

10. **J. Kim**, J.-H. Na, and S.-D. Lee, "Fully continuous liquid crystal diffraction grating with alternating semi-circular alignment by imprinting", *Opt. Express* **20**, 3034 (2012).

## [2] Domestic Journals

1. **J. Kim**, S.-U. Kim, B.-Y. Lee, J.-H. Suh, and S.-D. Lee, "Lenticular lens array based on liquid crystal with a polarization-dependent focusing effect for 2D-2D image applications", *J. Inf. Disp.* **16**, 11 (2015).

## [3] International Conferences

1. S.-U. Kim, E.-S. Yu, I.-H. Lee, **J. Kim**, and S.-D. Lee, “Fabrication of in-cell color patterns based on reactive mesogens for reflective liquid crystal displays”, *16th Topical Meeting on Optics of Liquid Crystals*, Sopot, Poland (2015).

2. B.-Y. Lee, **J. Kim**, and S.-D. Lee, “Flexible pressure sensor array based on highly elastic porous film”, *The 15th International Meeting on Information Display*, Daegu, Korea (2015).

3. S.-U. Kim, **J. Kim**, J.-H. Suh, B.-Y. Lee, and S.-D. Lee, “New vertical alignment mode of liquid crystal display with reduced gamma distortions by periodic patterns of reactive mesogens on alignment layer”, *The 15th International Meeting on Information Display*, Daegu, Korea (2015).

4. H. Kim, **J. Kim**, I.-H. Lee, and S.-D. Lee, “Liquid crystal-based lenticular lens array with laterally shifting capability of focusing”, *The 26th International Conference on Molecular Electronics & Devices*, Seoul, Korea (2015).

5. E.-S. Yu, S.-U. Kim, J.-H. Suh, **J. Kim**, and S.-D. Lee, “Dependence of the electro-optical properties of vertically aligned liquid crystal device by domain separation of reactive mesogens”, *The 4th Symposium on Liquid Crystal Photonics*, Shenzhen, China (2015).

6. S.-D. Lee, **J. Kim**, S.-U. Kim, B.-Y. Lee, and J.-H. Suh, "Realization of 2D/3D switchable displays with tunable lens array", *The 4th Symposium on Liquid Crystal Photonics*, Shenzhen, China (2015).

7. J.-H. Suh, B.-Y. Lee, **J. Kim**, S.-U. Kim, and S.-D. Lee, "Wide-range control of liquid crystal anchoring energy based on siloxane oligomer transfer", *The 2nd Asian Conference on Liquid Crystals*, Busan, Korea (2015).

8. **J. Kim**, S.-U. Kim, B.-Y. Lee, J.-H. Suh, and S.-D. Lee, "Imprinted lenticular lens array based on liquid crystal for autostereoscopic 2D/3D switchable displays", *The 14th International Meeting on Information Display*, Daegu, Korea(2014).

9. J.-H. Suh, **J. Kim**, and S.-D. Lee, "Control of liquid crystal pretilt by thermally assisted-transfer of siloxane oligomers during contact printing", *25th International Liquid Crystal Conference*, Dublin, Ireland (2014).

10. S.-U. Kim, **J. Kim**, E.-S. Yu, B.-Y. Lee, and S.-D. Lee, "Multi-directional colloidal assembly on wrinkled liquid crystalline polymer template", *25th International Liquid Crystal Conference*, Dublin, Ireland (2014).

11. **J. Kim**, J.-H. Suh, S.-U. Kim, and S.-D. Lee, "All-optically switchable grating based on dye-doped ferroelectric liquid crystal in photo-polymerized structure", *25th International Liquid Crystal Conference*, Dublin, Ireland (2014).

12. B.-Y. Lee, **J. Kim**, S.-U. Kim, and S.-D. Lee, “Capacitive pressure sensor based on porous hydrophobic elastomer for flexible electronic applications”, *European Materials Research Society Spring Meeting*, Lille, France (2014).

13. **J. Kim**, S.-U. Kim, E.-S. Yu, and S.-D. Lee, “Emerging areas for liquid crystal technologies beyond displays”, *SID Display Week*, San Diego, California, USA (2014).

14. S.-D. Lee, **J. Kim**, and S.-U. Kim, “How to design liquid crystal-based lenses for display applications”, *The 3rd Symposium on Liquid Crystal Photonics*, Shanghai, China (2014).

15. S.-D. Lee, **J. Kim**, and S.-U. Kim, “From optical devices to biological applications of photo-reactive mesogens”, *15th Topical Meeting on Optics of Liquid Crystals*, Honolulu, Hawaii, USA (2013).

16. S.-U. Kim, J.-H. Na, **J. Kim**, and S.-D. Lee, “Axially symmetric polarizers based on photoreactive mesogens through fluidic engraving”, *15th Topical Meeting on Optics of Liquid Crystals*, Honolulu, Hawaii, USA (2013).

17. **J. Kim**, S.-U. Kim, B.-Y. Lee, and S.-D. Lee, “Electrically switchable square lens array based on liquid crystals”, *15th Topical Meeting on Optics of Liquid Crystals*, Honolulu, Hawaii, USA (2013).

18. S.-U. Kim, J.-H. Na, **J. Kim**, and S.-D. Lee, “Precise lens-on-lens architecture using selective wettability for image-depth representation”,

*The 13th International Meeting of Information Display*, Daegu, Korea (2013).

19. B.-Y. Lee, S. C. Park, M.-H. Kim, **J. Kim**, and S.-D. Lee, "Highly pressure-sensitive capacitive sensors based on porous elastomers for touch panel applications", *The 13th International Meeting on Information Display*, Daegu, Korea (2013).

20. **J. Kim**, S.-U. Kim, B.-Y. Lee, and S.-D. Lee, "Liquid crystal-based hybrid optical retarder varying a quarter-to-half wave for three-dimensional displays", *The 13th International Meeting on Information Display*, Daegu, Korea (2013).

21. S.-U. Kim, J.-H. Na, **J. Kim**, and S.-D. Lee, "Radial polarizer with continuous optic axis using selective wetting inscription based on a liquid crystalline polymer", *SPIE Photonics West*, San Francisco, California, USA (2013).

22. S.-D. Lee, J.-H. Na, **J. Kim**, S. C. Park, and S.-U. Kim, "Tunable liquid crystal lens array for three-dimensional displays", *4th Workshop on Liquid Crystals for Photonics*, Hong Kong (2012).

23. **J. Kim**, J.-H. Na, and S.-D. Lee, "Effect of alignment symmetry and cell geometry on diffraction properties of liquid crystal grating", *24th International Liquid Crystal Conference*, Mainz, Germany (2012).

24. J.-H. Na, S. Lee, **J. Kim**, and S.-D. Lee, "Short focal length liquid crystal lens by encapsulation with photo-reactive polymer", *24th International Liquid Crystal Conference*, Mainz, Germany (2012).

25. **J. Kim**, E. Jang, K.-I. Joo, H.-R. Kim, and S.-D. Lee, "Dynamic polarization grating effect controlled by a single beam in a dye-doped liquid crystal", *The 16th International Symposium on Advanced Display Materials & Devices*, Jeju, Korea (2012).

26. S.-U. Kim, J.-H. Na, **J. Kim**, and S.-D. Lee, "Fabrication of polymer-based dual microlens with high numerical aperture through UV inscription and selective wetting", *International Symposium on Electronic/Optic Functional Molecules*, Shanghai, China (2012).

27. **J. Kim**, J.-H. Na, and S.-D. Lee, "Continuous diffraction grating based on a nematic liquid crystal with semi-radial alignment for display applications", *The 11th International Meeting on Information Display*, Goyang, Korea (2011).

28. **J. Kim**, J.-H. Na, and S.-D. Lee, "Graded-subdomain diffraction grating based on a nematic liquid crystal with semi-radial alignment", *SPIE Optics and Photonics*, San Diego, California, USA (2011).

29. S. Lee, **J. Kim**, J.-H. Hong, and S.-D. Lee, "Fabrication of electrically tunable liquid crystal lens arrays through selective wetting process", *The 22nd International Conference on Molecular Electronics and Devices*, Pohang, Korea (2011).

## [4] Domestic Conferences

1. **J. Kim**, S. Kim, and S.-D. Lee, “Continuous diffraction grating based on a nematic liquid crystal with semi-circular alignment”, *The 13th Korea Liquid Crystal Conference*, Gyeongsan, Korea (2011).
2. J.-H. Hong, **J. Kim**, and S.-D. Lee, “Fabrication of color filters through selective wetting process”, *The 13th Korea Liquid Crystal Conference*, Gyeongsan, Korea (2011).

# Abstract (Korean)

최근 디스플레이, 광통신, 광 데이터 프로세싱과 같은 광학계의 사용이 폭발적으로 증가하면서, 더 정교한 기능들의 필요성이 이러한 광학계에서 대두되었다. 따라서 광학계에 조금 더 특별하고 진보한 기능들을 부여하기 위해, 회절격자, 렌즈, 빔 분리기, 프리즘, 광 필터와 같은 광학계 내에서 중요한 역할을 하는 기본적인 광학부품에 대한 연구가 활발하게 진행되었다. 앞서 설명한 몇 개의 기본적인 광학부품 중에 특히 회절격자와 렌즈들이 규칙적으로 배열된 렌즈 어레이가 넓은 응용범위와 비교적 간단한 구동원리 및 구현 때문에 가장 활발하게 연구되는 중요한 기본적인 광학부품으로 간주되었다. 최근의 광학계에 있어서는 조정 기능이 필수적이기 때문에, 회절격자나 렌즈 어레이에 있어서도 외부 자극에 의해 광학특성을 변화시키는 기능이 요구되고 있다. 최근 몇 십 년 동안, 다양한 형태의 조정 가능한 회절격자나 렌즈 어레이가 제안되어왔고, 이들 중 대부분의 소자에서, 광학특성은 인가 전압, 입사하는 전자기파, 혹은 인가 압력에 의해 조정되었다. 특히, 액정의 우수한 광학적 이방성과 전기적 혹은 광학적 조정 가능성으로 인한 전기광학적 변환에 기반하여 많은 조정 가능한 회절격자나 렌즈 어레이가 액정을 사용하여 제작되어 왔다. 그러나 액정 회절격자는 자유로운 액정 배향이 어렵기 때문에 회절 패턴이

매우 제한적이고, 회절격자가 빛으로 조정될 때는 그 속도가 다소 느리고 회절 특성의 조정 범위도 작다는 문제점을 지니고 있다. 또한 액정 렌즈 어레이의 경우, 평평하지 않은 표면 위에서 액정 배향이 매우 어렵고 다른 형태의 렌즈에 비해 집광효과가 다소 제한되었기 때문에 그 응용이 제한되고 있다.

본 논문은 새로운 유형의 액정 회절격자와 액정 렌즈 어레이를 제안하는 것을 목표로 한다. 본 논문은 크게 세 부분으로 이루어져있다. 첫 번째와 두 번째 부분은 각각 전기적으로 조정 가능한 액정 회절격자와 빛으로 조정 가능한 강유전성 액정 회절격자에 대한 내용을 다룬다. 마지막 세 번째 부분은 전기적으로 조정 가능한 정사각형 모양의 액정 렌즈 어레이와 액정 렌티큘러 렌즈 어레이에 대해 다룬다.

첫 번째로, 셀의 두께에 관계없는 회절 특성을 보여주고 액정이 준 원형으로 배향된 영역을 가지는 완전히 연속적인 액정 회절격자를 제안한다. 회전적인 대칭성을 가지는 액정 회절격자의 연속적인 위상 조정은 마이크로 임프린팅된 표면 위에 준 원형으로 배향된 액정들을 통해 얻을 수 있었다. 본 액정 회절격자는 액정이 내부에서 하이브리드 형태를 이루고 있고, 완벽히 연속적인 위상 지연을 보여주며, 인가전압에 따라 회절 특성을 변화시킬 수 있다. 또한 입사광의 편광방향에 따라 회절된 빛이 서로 다른 두 개의 대칭성을 가짐을 보여주었다.

두 번째로, 서로 다른 광학 특성을 가지는 두 개의 영역으로 이루어진 빛으로 조정 가능한 강유전성 액정 회절격자를 제안한다. 염료가 도핑된 강유전성 액정이 한 영역에서는 균일하게 배향되어 있으며 다른 영역에서는 반응성 메소겐을 사용하여 형성된 광경화된 고분자망에 스며든 형태이다. 이러한 강유전성 액정을 기반으로 하는 회절격자는 기존의 네마틱 액정을 기반으로 한 빛으로 조정 가능한 회절격자에 비해서 더 효과적이고 1 초 이내의 빠른 조정 특성을 보여주는데, 이는 염료 및 액정 분자들의 광학적 반응이 강유전성 액정의 층상 구조내부에서는 외부요인에 의해 덜 제한되기 때문이다.

마지막으로, 입사광의 편광상태에 따라 두 가지의 집광 형태를 보여주는 액정 기반의 정사각형 렌즈를 제안한다. 사각형 모양의 투명한 고분자 렌즈 위에 액정이 한 방향으로 배향된 형태이며, 액정의 장축과 폴리머의 굴절상수가 같은 값을 지니도록 설계하였다. 따라서, 액정의 방향과 평행한 방향으로 편광된 입사광의 초점거리는 전기적으로 조정 가능하며 액정의 방향과 수직한 방향으로 편광된 입사광의 초점거리는 인가 전압과 상관없이 일정하다. 간단한 임프린팅 공정을 통해 제작한 편광 의존성 집광 효과를 가지는 액정 기반의 렌티큘러 렌즈 어레이 또한 제안한다. 앞선 정사각형 렌즈와 마찬가지로 렌즈와 주변의 액정의 굴절상수 일치를 통해 편광 의존성이 구현되었다.

요약하자면, 연속적인 액정 배향 형태를 가지는 전기적으로 조정 가능한 액정 회절격자와, 우수한 변환 특성을 가진 빛으로 조정 가능한 강유전성 액정 회절격자와 같은 새로운 유형의 액정 회절격자가 본 논문을 통해 제안된다. 또한 본 논문은 완벽한 편광 의존성을 가진 전기적으로 조정 가능한 액정 기반의 정사각형 렌즈 어레이와 렌티큘러 렌즈 어레이 또한 보여준다. 이러한 진보한 기능을 가진 기본 광학소자는 다양한 형태의 정교한 광학계의 개발에 유용할 것이다.

주요어: 회절격자, 렌즈 어레이, 네마틱 액정, 염료가 도핑된 강유전성 액정, 반응성 메소겐, 임프린팅

학번: 2009-20783